Feedback loops involving ERK, AMPK and TFEB generate non-genetic heterogeneity that allows cells to evade anoikis

Saurav Kumar[1], Kishore Hari[2], Mohit Kumar Jolly[2], and Annapoorni Rangarajan[1*]

[1]Department of Molecular Reproduction, Development and Genetics, Indian Institute of Science, Bangalore-560012, India

[2]Centre for BioSystems Science and Engineering, Indian Institute of Science, Bangalore-560012, India

***Name and address for correspondence:** Prof. Annapoorni Rangarajan, Department of Molecular Reproduction, Development and Genetics, Indian Institute of Science, Bangalore 560012, Karnataka, India, Phone: 91-80-22933263; Fax: 91-80-23600999

E-mail: anu@iisc.ac.in

Running title

Non-genetic heterogeneity in matrix-detached cells

Keywords: AMP-activated protein kinase (AMPK), Extracellular signal-regulated kinase (ERK), Phosphoprotein enriched in astrocytes 15 kDa (PEA15), TFEB, Autophagy maturation, Anoikis.

Financial support: This work was majorly supported by grants from the Wellcome Trust-DBT India Alliance (IA) Senior Research Fellowship (500112/Z/09/Z) to AR.

Abstract

Some solid tumor cells escape death triggered by matrix-deprivation and cause cancer spread through metastatic growth. The role of phenotypic plasticity in this adaptation remains unknown. We recently identified a double-negative feedback loop between pAMPK (phospho-AMPK) and pAkt (phospho-Akt) that regulates the switch between attached and detached states of cancer cells. In this study, we show that matrix-detachment itself can give rise to two subpopulations with varying ERK signaling levels and autophagy flux. Cells with elevated ERK activity show autophagy maturation arrest leading to anoikis, whereas those with low ERK activity overcome this block and generate anchorage-independent colonies. Investigating upstream, we show a novel role of AMPK-mediated phosphorylation of PEA15 in inhibiting ERK activity by reducing the formation of MEK-ERK complex. Consequently, cells with higher AMPK activity have lower phospho-ERK, and this heterogeneity is reflected *in vivo*. Exploring downstream, we demonstrate that ERK inhibition leads to upregulation of TFEB, a major regulator of lysosome biogenesis and autophagy. Overexpression of TFEB not only rescues the defect in autophagy flux, but also re-inforces AMPK signaling, thus revealing a positive feedback loop between AMPK and TFEB. Mathematical modelling of this loop shows that it can give rise to two distinct cellular phenotypes – $pAMPK^{high}/TFEB^{high}/pERK^{low}$ and $pAMPK^{low}/ TFEB^{low}/pERK^{high}$ – and phenotype switching, thus offering a mechanistic basis for our observations for non-genetic heterogeneity in anoikis adaptation. Significantly, we observed these heterogeneous cell states in patient-derived circulating tumor cells also. Thus, our work unravels a novel feedback loop that can generate non-genetic heterogeneity within matrix-detached cancer cells; targeting such loops may offer novel therapeutic approaches for restricting metastasis and improving therapeutic efficacy.

Introduction

Epithelial cells require attachment to extracellular matrix (ECM) for proper growth and differentiation. In contrast, detachment of cells from the ECM results in apoptosis, termed as “anoikis” (*1*, *2*). However, some cancer cells can develop anoikis resistance essentially to survive during transit through circulation and subsequently seed metastasis (*3*) – the major cause of cancer-related deaths. Therefore, understanding the mechanisms that enable cancer cells to overcome anoikis will help identify novel therapeutic targets to restrict cancer spread.

Detachment of cells from the ECM is also known to induce autophagy (*4*). Macroautophagy (or simply autophagy) is an evolutionarily conserved catabolic mechanism for degradation of protein aggregates, damaged organelles and intracellular pathogens through lysosomal lysis (*5*). Originally thought of as a cell death mechanism (*6*), emerging evidence points to pro-survival role for autophagy, particularly in cells experiencing a variety of stresses including starvation, hypoxia, and anti-cancer therapeutics (*7*). Autophagy is a multistep and dynamical process starting with the induction of double-membranous structures called as autophagosome, followed by their maturation and fusion with lysosome, and culminating with the degradation of sequestered materials in autophagosome(*5*). The completion of the entire process is termed as autophagic flux; defects in various steps can lead to several diseases including neurological, cardiac and muscular pathologies (*8*). Although autophagy induction has been demonstrated in matrix-detached cells (*4*), the status and regulation of autophagic flux in matrix-detached cells and its implications in anoikis resistance remains poorly understood.

The crosstalk between autophagy and apoptosis has been proposed to give rise to bistability (*9*), i.e cells in two distinct signaling states, thus potentially generating non-genetic heterogeneity in a cell population. However, the existence and implications of such heterogeneity in anoikis resistance remain to be identified. Non-genetic heterogeneity can be generated via crosstalk between molecular pathways, the most common of which being a mutually inhibitory feedback loop (*10*), such as that between phosphorylated AMPK (pAMPK) and phosphorylated Akt (pAKT) identified in our previous study (*11*). Here, we investigate the crosstalk between AMPK and ERK signaling to facilitate progression through autophagy to enable anoikis resistance. Our study identifies a novel feedback loop between AMPK and TFEB regulated by ERK signaling and highlights its role in mediating non-genetic heterogeneity and adaptation to survival under matrix-deprivation stress. Targeting this loop may hold promise for the development of novel therapy towards treating metastatic disease.

Methods and material

Cell culture and transfection

Breast cancer cell lines MDA-MB-231, MCF7, and BT-474 (procured from ATCC in 2016 and validated by STR analysis) Cells were trypsinized and cultured for indicated time points on tissue culture dishes coated with 1% noble agar (Sigma-Aldrich) to mimic ECM-

detachment Pharmacological agents were added immediately after trypsinization and prior to plating onto noble agar coated dishes. Long-term anchorage independent (AI) colony formation assay was performed by mixing $1x10^5$ cells with 1.5% methylcellulose and layered on top of 1.5 % noble agar coated dishes.

Cell transfection was performed using Lipofectamine 2000 according to manufacturer's protocol. OptiMEM media was used for the transfection and changed to regular media 6 hours post transfection. Drugs (Puromycin or G418) for selection were used for generation of stable cells after 24 hours of transfection. MDA-MB-231 cells stably expressing mCherry-EGFP-LC3, GFP-LC3, $EGR_{(promoter)}$-TurboRFP, pEGFP-TFEB, Scr (Control), or shTFEB#C5 were generated by transfection followed by FACS sorting.

Pharmacological compounds

Pharmacological compounds used in the study include compound C (10mM; Calbiochem), PD98059 (10 µM; CST), and rapamycin (100nM; Sigma-Aldrich). Dimethyl sulfoxide (DMSO, Thermo Scientific) was used as vehicle control for all the compounds except rapamycin, which was dissolved in ethanol.

Caspase 3-activity assay

Briefly, 1×10^6 cells were incubated with 1 µL of Red-DEVD-FMK for 30 minutes at 37°C incubator maintaining 5% CO_2. Caspase-3 activity was analysed by BD FACS-CantoII (Becton & Dickinson) containing a 488-nm Coherent Sapphire Solid State laser. Red fluorescence emission from cells was measured upon excitation with blue (488nm) laser. Post-acquisition data was analysed using Summit software V5.2.1.12465.

Immunoblotting

Whole cell lysates were prepared using 1X RIPA buffer containing 20 mM Tris-HCl (pH 7.5) 150 mM NaCl, 1 mM Na2 EDTA, 1 mM EGTA, 1% NP-40, 1% sodium deoxycholate, 2.5 mM sodium pyrophosphate, 1 mM β-glycerophosphate, 1 mM Na_3VO_4 and protease inhibitor on ice. Protein concentration was estimated by Bradford method and equal quantity was loaded on SDS-PAGE after boiling at 100°C for 5 minutes. Proteins were transferred to PVDF and probed for indicated primary antibodies. For multi-panel blots, PVDF membranes were stripped by boiling in 100nM EDTA for 5 min, subsequently re-probed with indicated

antibodies after blocking. Tubulin was used as loading control each time a given lysate was probed. Individual band intensity was quantified using Image-J software and was normalized to Tubulin.

Antibodies used in the experiments are pERK1/2, pMEK1/2$^{S217/S221}$, pACC^{S79}, pAkt^{S473}, pPEA15^{S116}, tERK, tMEK, ACC, Akt, tPEA15, TFEB, myc tag, HA tag, cleaved PARP, LC3, IgG (Cell Signaling Technology), α Tubulin (Calbiochem), PHLPP2 (Abcam), Flag-tag (Sigma-Aldrich), LAMP2 (Abcam), p62 (Cell Signaling Technology) followed by HRP-tagged secondary antibody (Jackson ImmunoResearch). Chemiluminescence (using ECL substrate from Thermo Fisher Scientific) image was acquired by Syngene G-Box bio imaging system.

Immunoprecipitation

For co-immunoprecipitation, cells were lysed in IP-lysis buffer containing 25 mM Tris, 150 mM NaCl, 1 mM EDTA, 1% NP-40, 5% glycerol (pH 7.4). Lysates (1.5mg) were incubated with IgG control, anti-Flag, or anti-PEA15 antibody and 15 µL of protein-A sepharose beads for 12 hours at 4°C on end-on rocker. The immune complexes were washed with Nonidet P-40 lysis buffer (25 mM Tris, 150 mM NaCl, 1 mM EDTA, 1% NP-40, 5% glycerol; pH 7.4) for 5 times. Immunocomplexes were analysed by immunoblotting.

Immunofluorescence

Immunofluorescence on attached and suspension cells were done as described previously (*12*). Briefly, cells in attached condition were fixed on dish by 4% PFA at room temperature for 10 minutes. Suspension cells were collected in 1.7 ml tubes and centrifuged at 3000 rpm for 3 min followed by 4% PFA fixation at room temperature for 10 minutes and spotted on coated glass slide. Permeabilization was carried out by 0.1 % triton X 100 for 15 minutes. Primary antibody diluted in PBST was added on cells and incubated overnight at 4°C or 2 hours at room temperature followed by incubation with fluorophore-tagged secondary antibody for 45 minutes at room temperature. Images were acquired using Olympus FV10i confocal laser scanning microscope after mounting the samples.

Co-localization analysis

The quantitative co-localization analysis of LAMP2 and GFP-LC3 was performed using Coloc-2 plugin in ImageJ program (NIH Image). For analysis, images of 30-40 cells were taken from multiple independent experiments (n=3). Each dot in the plots represents Pearson's correlation coefficient (PCC) value of LAMP2 and GFP-LC3 from a single cell. PCC is a statistical measure of the strength of the linear relationship between two data sets. Its value ranges from -1 to +1, with -1 representing negative co-relation, 0 no-co-relation and +1 represents a complete positive correlation.

Real-Time qPCR analysis

TRIzol reagent was used for isolation of total RNA. cDNA was prepared using random hexamer primers. Quantitative PCR was performed in Mastercycler RealPlex2 machine (Eppendorf) by using the KAPA SYBR FAST (Sigma-Aldrich). The primer sequence used in the study are: cFOS Forward primer: 5'AGTTCATCCTGGCAGCTCAC-3' and cFOS Reverse primer: 5' TGCTGCTGATGCTCTTGACA-3'.

Immunohistochemistry (IHC)

Day 7 lactating mammary gland was fixed in formalin, paraffin embedded and sectioned onto charged slides (Hisure Scientific). Slides were kept in air oven at 65°C overnight. Xylene was used to remove paraffin that is followed by rehydration in decreasing concentration of ethanol (100-70%). Tris-EDTA (pH 9) was used for antigen retrieval and 3% H_2O_2 solution for 20 minutes was used for neutralizing endogenous peroxidases. Primary antibody was incubated overnight at 4°C. Enhancer and secondary antibody were used as described by manufacturer's instruction (Biogenex Supersensitive polymer HRP IHC detection kit). Diaminobenzidine (DAB) was used as substrate for peroxidase, while counterstain was done with haematoxylin. Images were acquired by IX71 Olympus inverted microscope.

Experimental setup for metastasis studies

EAC cells were cultured in suspension with RPMI media (with 10% FBS) for 48 hours in noble agar coated dish along with DMSO, as vehicle control, or PD98059. Viable cells ($1x10^5$) were taken based on trypan blue exclusion staining and injected intraperitoneally in Swiss albino mice. Intraperitoneal injection of PD98059 was given on every alternate day till 15 days followed by dissection of lung after scarifying the animals. Tissues were fixed in

paraformaldehyde and embedded in paraffin followed by thin sectioning. Lung metastasis was analysed on H&E stained slides of the tissue section. Images were taken using I X 71 Olympus inverted microscope.

Microarray data analysis

MDA-MB-231 cells were cultured for 24 hours in attached or matrix-deprived condition and MDA-MB-231 cells stably expressing shAMPKα2 cultured in suspension condition. Microarray assay was done after harvesting cells at indicated time points. RNA isolation was performed using RNeasy minikit (Cat No. 74104; Qiagen). Cy3 labelling was done by Agilent's Quick-Amp labeling Kit (Cat. No. 5190-0442) followed by hybridization on Agilent's In situ Hybridization Kit (Cat No.5188-5242). The comparison was done between expression of same genes across test sample and control sample. The list of signature genes were selected from AmiGO Gene Ontology Consortium (http://amigo.geneontology.org/amigo), Profiler PCR Array list Qiagen, and further validated by KEGG (http://www.genome.jp/kegg/pathway.html) or PubMed (https://www.ncbi.nlm.nih.gov/pubmed/). The heat map of signature genes was created using online tool Morpheus (https://software.broadinstitute.org/morpheus/#). Downregulated genes were color coded in “green” and upregulated genes in “red”. The enriched altered pathways in the suspension culture, were determined by Gene Set Enrichment Analyses (GSEA).

RNA sequencing data for single-CTC and cluster-CTCs were taken from Gene Expression Omnibus (GEO; ID: GSE51827). The raw value was converted into $\log_2$ value. Box plots for the value of signature genes were plotted using GraphPad Prism 5.0 software.

Mathematical modelling

A mathematical model was constructed to depict the interaction between pAMPK, pERK and TFEB using a set of three coupled ODEs that consider the timescale separated kinetics of protein phosphorylation/dephosphorylation and protein production processes. Kinetic rate constants were estimated from previous studies and current work. A detailed description of the model is presented in the supplementary text. Nullclines and bifurcation plots were generated using MATLAB (Mathworks Inc.).

Statistical Analysis

GraphPad Prism V software was used to plot graph and analyse statistical significance of the data by using student's t-test. Each experiment was performed at least thrice and one is being represented in the figures. All data are presented as mean ± standard error of the mean (SEM). *P* value below 0.05 was considered as statistically significant; ***represents $P \leq 0.001$, **represents $P \leq 0.01$ and *represents $P \leq 0.05$.

Results

ERK signaling heterogeneity in matrix-deprived cells

In matrix-deprived cells, both increased ERK activity and a loss of ERK activity has been reported in different cell types (*13-15*). In light of these contrasting reports, we checked the status of ERK signaling in breast cancer cells that were subjected to matrix-detachment for short (24 hours) in suspension and long (one week) in methylcellulose. Analysis of our previously performed transcriptomics data (*11*) on MDA-MB-231 breast cancer cells cultured in adherent (attached, Att) versus matrix-deprived (suspension, Sus) conditions for 24 hours showed increased expression of genes involved in ERK signaling in suspension **(Figure 1A)**. GSEA analysis confirmed induction of the ERK pathway in suspension **(Figure 1B)**. To further confirm ERK activation, we measured levels of phosphorylated ERK (henceforth referred to as pERK) using phospho-ERK (Thr^{202}/Tyr^{204})-specific antibodies which serves as a surrogate for ERK activity. We observed elevated pERK levels by immunoblotting in multiple breast cancer cell types, such as, BT-474, MDA-MB-231, and MCF-7, when cultured in suspension for 24 hours **(Figures 1C, S1A & S1B,** respectively**)**. Levels of total ERK remained unaltered between these two conditions **(Figures 1C, S1A & S1B)**. Further, we also observed increase in *cFOS* expression **(Figure 1D)** and Egr1-promoter activity **(Figure 1E)** in matrix-deprived condition. Together, these data suggested elevated ERK signaling in breast cancer cells that were matrix-detached for 24 hours.

We next gauged the status of ERK signaling upon long-term culture (one week) under matrix-deprivation that leads to the formation of anchorage-independent cancer spheres. Intriguingly, immunoblotting of cancer spheres revealed a significant reduction in pERK levels compared to adherent cultures **(Figure 1F)**. Since only a subpopulation of cancer cells survive the matrix-deprivation stress to generate anchorage-independent colonies, based on our observations, we hypothesized a possible heterogeneity of ERK activity in matrix-deprived cells such that those with lower ERK activity have better fitness to overcome anoikis and generate colonies.

To test this hypothesis, we first checked the status of ERK signaling in individual cells by immunocytochemistry for pERK. We indeed observed heterogeneity in pERK levels in matrix-detached cells by immunocytochemistry (**Figures 1G & S1D.a).** We further confirmed ERK signaling heterogeneity using the Egr-1 TurboRFP promoter-reporter system (**Figures 1H & S1D.b**) in which the Egr-1 promoter is driven by MEK/ERK signaling, and serves as a measure of ERK activity (*16*). Interestingly, while we observed a basal heterogeneity of ERK activity within the adherent population, in response to matrix-deprivation, both endogenous pERK staining as well as Egr-1 promoter activity based assay **(Figures 1G and H)** revealed the emergence of a new population of cells with elevated, yet heterogeneous ERK activity (**Figure S1D**).

Using flow cytometry, we further sorted this population based on Egr-1 promoter activity into low and high RFP cells **(Figure 1I.a)**. Immunoblotting confirmed higher pERK levels in high-RFP cells compared to low-RFP cells **(Figure 1I.b)**. We then sought to test the role of ERK signaling heterogeneity in the regulation of cellular fitness under matrix-detachment stress. Consistent with our hypothesis, the high-RFP cells showed more anoikis, as revealed by higher caspase 3 activity **(Figure 1J)**. Supporting this, a kinetic study of matrix-detached cells showed a decrease in the RFP-high cells over a week **(Figure S1E)**. Further, these cells also generated less anchorage-independent colonies compared to RFP-low cells **(Figure 1K)**. Thus, matrix-detachment leads to heterogeneous ERK activation, with low ERK activity being more conducive for survival under matrix-detachment conditions.

ERK signaling heterogeneity regulates autophagy maturation in matrix-detached cells

Next, we investigated what biological processes might be perturbed by ERK signaling and its role in regulating anoikis. Stress induces autophagy which, in turn, is known to regulate apoptosis (*17*). Autophagy induction has been reported in matrix-detached cells and also shown to aid anoikis-resistance (*4*). Meanwhile, ERK signaling is known to independently regulate both autophagy and anoikis (*14, 18*). Therefore, we sought to investigate the role of ERK signaling heterogeneity in the regulation of autophagy and anoikis under matrix-deprivation.

Although autophagy induction has been reported in matrix-detached cells (*4*), little is known about the downstream processes. To better comprehend the autophagic process in matrix-deprived cells, we first undertook a detailed analysis of the various steps of autophagy in breast cancer cells that were subjected to matrix-deprivation for 24 hours. During autophagy,

LC3 is cleaved to form a truncated soluble form named LC3-I, which is then lipidated to form LC3-II that binds to the autophagosome membrane, and thus, serves as a marker for autophagosomes (*19*). We observed an increase in the levels of LC3-II in matrix-deprived cells compared to attached cells by immunoblotting **(Figure 2A)**. We also observed an increase in the protein levels of Beclin1 **(Figure 2A)**, which plays a key role in autophagy induction (*20*). These data confirmed induction of autophagy in matrix-deprived cells as shown before (*4*).

We next investigated the turnover or flux of autophagy in matrix-deprived cells by measuring the levels of p62/SQSTM1, an LC3-interacting protein that is degraded in the autolysosome (*21*). Interestingly, we observed accumulation of p62 in matrix-deprived condition **(Figure 2A)**. An increase in LC3-II together with accumulation of p62 is suggestive of a blockage in autophagic flux (*22*). To better gauge autophagic flux, we used the tandem-labelled mCherry-EGFP-LC3 construct (*7*). In this system, the autophagosomes are seen as yellow puncta (because of both mCherry and EGFP fluorescence), whereas after fusion with lysosome, the autolysosomes are seen as red puncta (because of quenching of EGFP by the acidic nature of lysosome) (*23*). Treatment with rapamycin served as a positive control for autophagy flux, leading to an increase in red puncta compared to basal autophagy in adherent cells **(Figure 2B)**. Interestingly, despite induction of autophagy, a large number of matrix-deprived cells showed yellow puncta, suggestive of reduced autophagic flux **(Figure 2B).** We further quantified the red and green signal per cell to express as mCherry/EGFP ratio, which serves as a good measure of autophagy flux (*24*). Compared to rapamycin treated cells that showed an elevated mCherry/EGFP ratio, indicative of high autophagic flux, matrix-deprived cells showed less mCherry/EGFP ratio, indicative of low autophagic flux (Graphs in **Figures 2B and S2A**). Furthermore, our data revealed autophagy flux heterogeneity in matrix-detached cells with majority showing yellow puncta (yellow arrow), while some cells showed red puncta (red arrow, **Figure 2B**). Staining for p62 in matrix-deprived cells further confirmed this heterogeneity **(Figure 2C)**.

Failure of fusion of autophagosomes with lysosomes can impair autophagic flux (*25*). To test if this could be a cause of reduced autophagy flux in matrix-detached cells, we performed immunostaining for LAMP2, a lysosomal marker (*25*), and gauged its co-localization with GFP-LC3 puncta that is indicative of autophagosome-lysosome fusion (*26*) using confocal microscopy. Quantitative co-localization analysis (as described in methods) revealed less LAMP2/LC3 co-localized punctae in a large proportion (~70%) of matrix-deprived cells

(Figures 2D &S2B), suggestive of blocked autophagy maturation in these cells. Induction of autophagy but blockade of maturation has been shown to lead to apoptosis (*27*). To gauge this, we compared the levels of cleaved caspase 3 (a marker of apoptosis) with accumulation of p62 (a marker of blocked autophagy) by immunocytochemistry (**Figure 2E**). A Spearman's correlation analysis revealed a positive correlation between cleaved caspase 3 and p62 levels (**Figure 2E**). In contrast, we observed less accumulated p62 in cancer spheres **(Figure S2C)**. Thus, these data revealed a co-relation between autophagy maturation arrest and anoikis.

Having identified ERK signaling heterogeneity in matrix-detached cells, and establishing a model to isolate high and low ERK activity MDA MB 231 cells **(Figure 1I)**, and having previously observed more anoikis in RFP-high ($pERK^{high}$) cells, we investigated the status of autophagy maturation in these two populations. When RFP-high and RFP-low cells were subjected to matrix-deprivation, we observed that the RFP-low cells showed reduced LC3-II and p62 levels by immunoblotting **(Figure 2F),** and increased co-localization of GFP-LC3 and LAMP2 by confocal microscopy **(Figure S2D)**, indicative of higher autophagic flux compared to the RFP-high cells. Immunocytochemistry for p62 further supported this data as it showed a positive co-relation between high GFP and p62 accumulation **(Figure 2G)**. Collectively, these observations reveal an association between ERK signaling heterogeneity and autophagy maturation which in turn regulates cell fate: cells with low ERK activity have higher autophagy flux and show better survival fitness under matrix-deprivation.

ERK inhibition increases autophagy flux and anoikis resistance

ERK signaling is known to regulate various steps of autophagy, both positively and negatively, in different cellular contexts (*18, 28*). Our data above revealed an inverse correlation between high ERK activity and autophagy maturation. To better understand how ERK signalling impinges on autophagy flux in matrix-detached cells, we gauged the effect of ERK inhibition on autophagy maturation and anoikis. Treatment of matrix-deprived cells with MEK inhibitor PD98059 resulted in reduced pERK levels (**Figure 3A**); additionally, we observed a decrease in the levels of LC3-II together with p62 in these cells **(Figure 3A)**. We observed similar result in yet another breast cancer cell line, BT-474 **(Figure S3A)**. We further used a genetic approach to reduce ERK levels by overexpressing dominant-negative form of MEK1 (MEK1-K97A). We observed a decrease in the levels of pERK, LC3-II and p62 in these cells **(Figure 3B);** decrease in LC3-II together with that of p62 is indicative of

increased autophagic flux. Visualization of red punctae in matrix-deprived cells expressing the mCherry-GFP-LC3 flux construct further confirmed this **(Figure 3C)**. Furthermore, we observed an increase in the number of cells showing co-localization of LAMP2 with GFP-LC3 upon ERK inhibition **(Figure 3D)**, together revealing progression through autophagy upon ERK inhibition. Consistent with this, we observed a reduction in anoikis upon ERK inhibition, as revealed by a decrease in the levels of cleaved PARP (**Figures 3E & S3B**) and reduced caspase 3 activity **(Figure 3F).** Given the key role played by anoikis resistance in cancer metastasis, we further tested the significance of down modulation of ERK signaling in murine experimental metastasis model using Ehrlich Ascites Carcinoma (EAC) cells. Intraperitoneal injection of EAC cells that were treated with PD98059 led to increased number of metastatic nodules **(Figure 3G)**, thus supporting our *in vitro* data showing enhanced anoikis-resistance upon ERK inhibition.

AMPK inhibits ERK activity upon matrix-deprivation

We next sought to understand what might regulate ERK activity in matrix-detached cells. Work done by our laboratory and that of others has identified AMPK activation as a critical aspect of survival of cells under matrix-deprivation (*11, 12, 29, 30*). In different contexts, AMPK is known to either activate or inhibit ERK activity (*31, 32*). To investigate if AMPK played a role in regulating ERK phosphorylation in matrix-detached cells, we first checked for AMPK activity, as measured by levels of its phosphorylated bonafide substrate ACC, in the RFP-high and RFP-low cells by immunoblotting. Interestingly, we observed an inverse co-relation between AMPK and ERK activities, such that the RFP-high ($pERK^{high}$) cells showed less pACC levels and vice versa **(Figure 4A)**. Quantitative immunofluorescence analysis of matrix-detached MDA MB 231 cells further confirmed this inverse correlation between AMPK activity and pERK levels **(Figure 4B)**. To further test this *in vivo*, we resorted to the lactating female mammary gland (*9*). The matrix-deprived luminal cells of the lactating mammary gland also showed inverse correlation between pAMPK and pERK status **(Figure 4C)**. Also, in human breast cancer patient samples, we observed heterogeneity of ERK signaling, as well as regions showing inverse correlation between AMPK activity and pERK levels **(Figure S4A)**. Taken together, these data suggested a possible negative regulation of ERK activity by AMPK.

In order to further address if AMPK is directly involved in negatively regulating ERK signaling in matrix-deprivation, we tested the effect of downmodulating AMPK activity on

pERK levels in matrix-deprived cells using pharmacological agents and genetic approaches. Treatment of matrix-deprived MDA-MB-231 cells with pharmacological inhibitor of AMPK, compound C (henceforth referred to as CC) led to a reduction in pACC levels **(Figure 4D).** Simultaneously, we observed an increase in pERK levels compared to vehicle DMSO treated cells **(Figure 4D)**, whereas CC had no effect on total ERK levels **(Figure 4D).** We observed similar effects in yet another breast cancer cell line BT-474 **(Figure S4B)**. To further confirm this using a genetic approach, we employed MEFs that are double knock out for AMPK α1/α2 (MEF-DKO). Compared to wild type (WT) MEFs, we also observed elevated pERK levels in MEF-DKO in suspension, whereas total ERK levels remained unaltered **(Figure 4E)**. Consistent with increased ERK phosphorylation, AMPK inhibition also led to an increase in *cFOS* gene expression **(Figure 4F)** as well as *Egr-1* promoter activity **(Figure 4G)**, confirming a negative regulation of ERK activity by AMPK in suspension.

We next investigated the significance of AMPK-ERK axis in regulating autophagic flux and anoikis of matrix-deprived cells. We have previously shown that AMPK activity is important for overcoming anoikis and that AMPK inhibition increases anoikis (*11*). Here, we observed that ERK inhibition decreases anoikis (**Figure 3F**), and our data further showed that AMPK inhibits ERK activity in matrix-detached cells. Based on these observations, we reasoned that AMPK-mediated ERK inhibition might be essential for anoikis. In this case, ERK inhibition should rescue the anoikis phenotype of AMPK inhibition. To test this, we investigated the effect of ERK inhibition on cells treated with AMPK inhibitor on their autophagy maturation and anoikis response. Inhibition of AMPK abrogated the co-localization of LAMP2 with GFP-LC3 puncta (**Figures 4H & S4C**), whereas simultaneous ERK inhibition restored this co-localization **(Figures 4H & S4C)**. Consistent with this observation, AMPK inhibition-mediated increase in anoikis {as reported by us previously (*11*)} was also rescued by co-treatment with PD98059, as revealed by a decrease in caspase-3 activity **(Figure 4I)**. Taken together, these data highlight the role of ERK signaling downstream to AMPK activation in regulating autophagy and anoikis.

AMPK-mediated phosphorylation of PEA15 regulates MEK-mediated ERK-activation

We next investigated the mechanisms involved in AMPK-mediated negative regulation of ERK in matrix-deprived condition. We failed to observe changes in the phosphorylation status of MEK, the upstream ERK kinase, upon matrix deprivation **(Figure S5A)** or upon AMPK inhibition **(Figure S5B)**. These data suggested that AMPK does not affect ERK

activity by altering MEK phosphorylation or via activation of Ras. Next, we gauged if AMPK activation affects MEK-ERK interaction.

Phosphoprotein enriched in astrocytes 15 kDa (PEA15) is a scaffold protein that is known to regulate the cytoplasmic localization of ERK (*33*). Earlier work from our laboratory identified AMPK as a direct upstream kinase of PEA15 in matrix deprivation leading to its phosphorylation at S116 position, which aids in alleviating anoikis (*29*). Interestingly, we observed higher S116 PEA15 phosphorylation in RFP-low ($pERK^{low}$) cells and vice versa **(Figure 5A)**, suggesting an inverse correlation between pERK levels and S116 phosphorylation of PEA15 in suspension. We investigated if AMPK-mediated phosphorylation of PEA15 at S116 influences ERK phosphorylation in matrix-deprived cells. As seen previously in anchorage-independent breast cancer spheres (*29*), we observed elevated S116 phosphorylation of PEA15 in MDA-MB-231 cells matrix-deprived for 24 hours **(Figure S5C)**. To directly address the role of S116 PEA15 phosphorylation, we used a Flag-tagged S116A mutant of PEA15 that cannot be phosphorylated at S116 position (*29*). MDA-MB-231 cells stably expressing Flag-tagged WT- (wild type) or S116A- PEA15 showed equal expression of these proteins when probed with flag antibody **(Figure 5B)**. The levels of total ERK remained unaffected between these cells under matrix deprivation. Interestingly, we observed elevated pERK levels in S116A-PEA15 expressing cells in suspension **(Figure 5B**); this change was not observed in adherent condition **(Figure S5D)**. Further, treatment with AMPK inhibitor compound C (CC) led to increase in pERK levels in matrix-deprived WT-PEA15 expressing cells, but not in S116A-PEA15 expressing cells **(Figure S5E)**. Together, these data identify a role for AMPK-mediated S116A-PEA15 phosphorylation in negatively regulating ERK phosphorylation in matrix-deprived cells.

We further investigated the mechanisms of negative regulation of ERK activity by AMPK-PEA15 signaling. Co-immunoprecipitation with Flag antibody in matrix-deprived MCF-7 cells transiently expressing Flag-tagged WT-PEA15 led to the detection of MEK and ERK by western blotting **(Figure 5C)**. We also observed the same in yet another breast cancer cell line, MDA-MB-231 cells, stably expressing Flag-tagged WT-PEA15 **(Figure S5F)**, suggesting the presence of a PEA15-ERK-MEK ternary complex in matrix-detached cells. Interestingly, compared to WT-PEA15 expressing cells, we observed increased association of MEK in S116A-PEA15 overexpressing cells in this complex **(Figure 5D)**. In keeping with elevated MEK association, we also observed higher levels of phosphorylated ERK in the Flag IP-western blots in the S116A-PEA15 expressing cells compared to WT-PEA15 expressing

cells **(Figure S5G)**, suggesting a possible role for S116A phosphorylated PEA15 in MEK-mediated ERK phosphorylation in suspension. Next, we checked the role of AMPK-mediated phosphorylation of endogenous PEA15 in its association with MEK, and ERK phosphorylation **(Figure 5F)**. Co-immunoprecipitation with PEA15-specific antibody followed by immunoblotting revealed an increase in the amount of MEK in CC treated cells compared to DMSO **(Figure 5F)**. Consistent with this data, pERK levels were also more in the cells treated with AMPK inhibitor (CC) **(Figure 5F)**. To further confirm role for PEA15, we undertook a genetic approach, using siRNA to deplete endogenous PEA15 levels. We observed decreased pERK levels upon knockdown of PEA15 (**Figure 5E)**, confirming a role for PEA15 in ERK phosphorylation in matrix-detached cells. Collectively, these data suggest that phosphorylation of PEA15 by AMPK in matrix-deprived cells hinders MEK-mediated ERK phosphorylation.

We next investigated the role of PEA15 phosphorylation in regulating autophagy flux and anoikis in matrix-detached cells. Compared to WT-PEA15 expressing cells, those expressing S116A-PEA15 showed elevated LC3-II and p62 levels under matrix-deprivation **(Figure 5G)**, suggesting autophagy maturation block; this block was in part relieved by treatment with ERK inhibitor PD98059 **(Figure 5G)**. Further, we observed a decreased co-localization of LAMP2 with GFP-LC3 in cells over-expressing S116A-PEA15 compared to WT-PEA15 expressing cells **(Figures 5H & S5H)**, whereas treatment with PD98059 restored LC3 co-localization with LAMP2 in these cells **(Figures 5H & S5H)**. These data suggested that AMPK-PEA15 axis mediated inhibition of ERK activity is needed to overcome the autophagy maturation block in matrix-deprived cells. Consistently, S116A-PEA15 expressing cells showed elevated caspase-3 activity under matrix-deprivation compared to WT-PEA15 expressing cells **(Figure S5I)**, which was alleviated by PD98059 treatment **(Figure S5J)**. Thus, in matrix-deprivd cells, the AMPK-PEA15 axis ameliorates autophagy flux by inhibiting ERK activity and promoting survival.

ERK inhibition leads to elevated TFEB levels

Having identified an AMPK-PEA15 axis upstream to the negative regulation of ERK activity in matrix-deprived cells, we investigated the events downstream of ERK inhibition that contribute to overcoming autophagy maturation block in these cells. Literature suggests that ERK phosphorylates and inhibits nuclear localization of transcription factor EB (TFEB), a master regulator of lysosomal biogenesis and autophagy (*34*). Therefore, we investigated if

ERK signaling affects TFEB localization in matrix-deprived cells using EGFP-tagged TFEB construct. We largely detected cytoplasmic localization of TFEB in both adherent and matrix-detached MDA-MB-231 cells **(Figure S6A)**. While inhibition of ERK led to nuclear translocation of EGFP-TFEB in adherent MDA-MB-231 and MCF-7 cells **(Figure S6B)**, ERK inhibition did not alter TFEB localization in either of these cell types in matrix-deprived cells **(Figures S6A and S6C)**, suggesting that the effect of ERK signaling in regulating autophagy maturation in matrix-detached cells may not be through altering TFEB nuclear localization.

Interestingly, though, we observed that matrix-detachment led to a reduction in the levels of exogenously expressed EGFP-TFEB **(Figure S6Aiii)**, suggesting a possible posttranslational regulation. Immunoblotting with TFEB-specific antibodies also revealed a reduction in endogenous TFEB levels upon detachment of MDA-MB-231 cells from the ECM **(Figure S6D)**. We also observed more TFEB levels in the RFP-low cells with lower ERK activity as compared to RFP-high cells **(Figures 6A & S6E)**, suggesting an inverse co-relation between ERK activity and TFEB levels. Consistent with this, ERK inhibition led to an increase in TFEB levels in matrix-deprived condition **(Figures S6A & 6B)**. We failed to detect changes in transcript levels of TFEB in the microarray data between adherent and detached cells **(Figure S6F)**, further suggestive of post translation regulation. TFEB protein stability is known to be regulated by a chaperone-dependent E3 ubiquitin ligase (*35*). Consistent with this mechanism, a cycloheximide chase assay revealed a decrease in TFEB protein stability in matrix-deprived cells, a decrease which was rescued by ERK inhibition **(Figure S6G)**. These data suggested that ERK signaling negatively regulates TFEB protein levels in suspension.

Motivated by our observations that AMPK is responsible for the negative regulation of ERK **(Figure 4)**, we checked the role of AMPK in the regulation of TFEB levels in suspension. We observed a reduction in the levels of TFEB upon inhibition of AMPK **(Figure 6C)**. Treatment with ERK inhibitor PD98059 rescued the effects of AMPK inhibition on TFEB levels **(Figure 6D)**, suggesting that matrix-detachment triggered AMPK upregulates TFEB protein levels in suspension culture by inhibition of ERK activity.

We next investigated the role of TFEB downstream of ERK in regulating autophagy maturation and anoikis-resistance. In matrix-deprived MDA MB 231 cells overexpressing EGFP-TFEB, we observed an increase in LAMP2 staining by immunofluorescence **(Figures 6E & S6H),** as well as increased co-localisation of LAMP2 with LC3-RFP **(Figures 6F &**

S6I), suggesting increased autophagic flux in these cells. Furthermore, TFEB overexpression rescued AMPK inhibition-mediated decrease in LAMP2 levels **(Figures 6G & S6J)**, autophagic-flux defect **(Figures 6F & S6I)** and anoikis **(Figure 6H)**. Reinforcing this data, TFEB overexpression led to a significant increase in the number of anchorage-independent colonies formed, as well as rescued the colony formation deficiency imposed by AMPK inhibition **(Figure 6I)**. Put together, these experiments emphasize that TFEB upregulation downstream of AMPK/ERK axis promotes autophagic flux to overcome anoikis resistance and promote anchorage-independent growth.

Double positive feedback loop between AMPK and TFEB mediated by ERK signaling generates bistability under matrix-deprivation

After investigating the molecular mechanisms of AMPK-mediated upregulation of TFEB levels via negative regulation of ERK, we were keen to explore whether TFEB regulates AMPK and/or ERK activities. This idea emerged from our observations of different subpopulations – $pAMPK^{high}/pERK^{low}/TFEB^{high}$ and $pAMPK^{low}/ pERK^{high}/TFEB^{low}$ **(Figures 1I, 4 & 6A)**, suggestive of systems with two cell states (bistability). Bistability usually emerges in cases of 'double positive' or 'double negative' feedback loops between a set of molecular factors (*36*). To address this possibility, we investigated possible cross talks between TFEB and AMPK/ERK signaling. Interestingly, in matrix-deprived MDA-MB-231 cells overexpressing EGFP-TFEB we observed increased phosphorylated (and active) AMPK, as well as elevated phosphorylation of its bonafide substrate ACC **(Figures 7A, 7B, & S7A)**. We observed increased AMPK activity in yet another cell line MCF7 overexpressing EGFP-TFEB **(Figure S7B)**. Consistent with increase in AMPK activity, we observed further decrease in pERK levels in these cells **(Figures 7A & S7B**). In addition, knockdown of TFEB resulted in decreased AMPK activity **(Figures 7C and S7C)** and increased pERK levels **(Figure 7C)**. We also observed decrease in LAMP2-levels, as well as a decrease in LC3 and LAMP2 co-localization, upon knockdown of TFEB (**Figures 7D, S7D, 7E, & S7E**). Collectively, these data underscore that TFEB positively regulates AMPK activity and lysosomal biogenesis, thus regulating autophagic flux.

Next, we investigated the mechanisms by which TFEB can activate AMPK in matrix-deprived condition. We have shown that calcium spike immediately after detachment contributes to increase in ROS production, in turn leading to AMPK activation (*12*). Therefore, we measured the levels of ROS upon overexpression of TFEB in suspension

culture using CellROX™ Deep Red reagent. Interestingly, we observed increased levels of ROS in TFEB overexpressing cells **(Figure S7F)**. In contrast, ROS levels decreased upon knockdown of TFEB **(Figure S7G)**. Furthermore, ROS inhibition by addition of NAC reduced AMPK activity in TFEB expressing cells cultured in suspension **(Figure 7F)**. Thus, our data suggested elevated ROS levels as one possible mechanism for TFEB-mediated induction of AMPK activity in in matrix-deprived condition.

Since overexpression of TFEB led to hyperactivation of AMPK and inhibition of ERK activity **(Figure 7A)**, while we previously saw ERK negatively regulates TFEB levels **(Figures 6A & 6E)**, thus we next checked the effect of ERK inhibition on AMPK activity under matrix deprivation. Indeed, ERK inhibition led to elevated AMPK activity **(Figures 7G, 7H, & S7H)**. Moreover, we observed decrease in AMPK activity in cells stably expressing S116A-PEA15 **(Figure S7I)** where we had observed higher ERK activity **(Figure 5D)**. Collectively, these data are suggestive of feedback loops involving AMPK, ERK, and TFEB.

We tested for three different potential feedback loops: **I)** TFEB inhibits ERK without involving AMPK (a 'double negative' one between ERK and TFEB), **II)** TFEB activates AMPK directly or indirectly (a 'double positive' one between AMPK and TFEB), and **III)** a combination of both of the above-mentioned possibilities **(Figure 8A)**. To test which of these feedback loops actually operates within matrix-detached cells, we measured the levels of pERK and pAMPK in TFEB overexpressing MDA-MB-231 cells, and that of pERK under AMPK inhibited condition in these cells. TFEB overexpression led to reduction in ERK activity and increase in AMPK activity **(Figure 8B)**; this observation can be explained by network II or III, but not by network I. Further, overexpression of TFEB combined with AMPK inhibition led to similar levels of pERK as in control cells **(Figure 8B; compare lane 4th with 1st)**, thus supporting network II. According to network III, the above-mentioned experiment **(Figure 8B)** would have led to a decrease in pERK levels, which we did not observe. Therefore, TFEB may activate AMPK through ROS and some yet unidentified players, leading to the formation of a 'double positive' feedback loop between pAMPK and TFEB, and consequently a decreased pERK activity **(network II) (Figure 8B)**.

We constructed a mathematical model capturing the interactions shown in network II. This network can give rise to two distinct cellular phenotypes – pAMPK^{high}/TFEB^{high}/pERK^{low} and pAMPK^{low}/ TFEB^{low}/pERK^{high} (shown by solid green circles in **Figures 8C & S8A**) as

observed in our experiments. Our mathematical model predicts that cells in these two states can also switch spontaneously, under sufficiently strong stochastic/noise perturbations, once they cross a 'tipping point' (shown by white circles in **Figures 8C & S8A**). This prediction is largely robust to parameter variation in the model (**Figure S8B**) and consistent with our experimental observations of a switch in phenotype upon overexpression or inhibition of TFEB (**Figure 7**). To test the prediction, we FACS sorted RFP-high and RFP low cells from MDA-MB-231/EGR1$_{promoter}$-TurboRFP expressing cells that were subjected to 24 hours of suspension. The sorted cells were then followed for a period of 24 and 48 hours of suspension, and tested for their ability to switch phenotype and generate the other population. Indeed, we observed such switching and a gain in heterogeneity over time in the sorted cells in matrix-deprived condition **(Figure 8D)**. Furthermore, cells with low ERK activity were able to attain the original heterogeneity much quicker than the cells with high ERK activity. Together, these results strongly indicate phenotypic switching, which can generate non-genetic heterogeneity in a given cell population.

To further understand the biological relevance of the AMPK-ERK-TFEB axis in metastatic human disease, we analysed the RNA-sequencing data of single circulating tumor cells (CTCs) and CTC-clusters derived from breast cancer patients (*37*). The observed heterogeneity in ERK/AMPK activities and TFEB levels in matrix detached breast cancer cells in vitro was captured *in vivo* **(Figures S8E & F)**. Interestingly, we observed higher association of AMPK and TFEB gene signature with CTC-clusters **(Figures 8E, & S8E)** that were reported to corroborate with increased metastasis and poor survival (*37*). Conversely, higher ERK gene signature was observed with single-CTCs **(Figures 8E & S8F)**. These data are in corroboration with our *in vitro* studies where we demonstrated that matrix-deprived breast cancer cells with pAMPK^{high}/pERK^{low} status express higher levels of TFEB and show better survival.

Discussion

Adaptation to matrix-deprivation is fundamental for successful metastasis. Further, phenotypic heterogeneity and plasticity within different cell populations of a cancer poses a major challenge to effective treatment strategy (*38*). Yet, the existence and implications of such heterogeneity in anoikis resistance remain to be identified. In this study, we demonstrate phenotypic (i.e. non-genetic) heterogeneity with respect to ERK signaling. The existence of such non-genetic heterogeneity is beginning to be reported more frequently due to high-

throughput techniques such as single-cell RNA-seq (*39, 40*), however, the origins and implications of such heterogeneity remain largely elusive. Our results here show how this heterogeneity emerges for ERK – through feedback loop among AMPK, ERK and TFEB. We show that the $AMPK^{high}/ERK^{low}/TFEB^{high}$ state enables overcoming autophagy maturation arrest, thus facilitating anoikis resistance. Thus, targeting this feedback loop might provide a novel and rational anti-cancer treatment strategy.

Autophagy is a cellular homeostasis mechanism in which cells recycle their nutrients at times of starvation and remove dysfunctional intracellular organelles (*6*). Initially, autophagy was thought of as a tumor suppressive mechanism, based on observations that *Beclin1* was deleted in most breast cancers and its overexpression in MCF7 cells reduced tumorigenesis (*20, 41*). Similarly, deletion of *Atg5* and *Atg7* in mice led to development of benign tumor (*42, 43*). However, autophagy is robustly activated in tumor cells facing stresses such as oncogenic insult, starvation, hypoxia, matrix deprivation, or higher metabolic demands (*43*). Consistently, we observed increased autophagy induction in matrix-deprived condition, detected by increased LC3-II levels. LC3-II levels can also increase due to the inhibition of its degradation in autolysosome. However, concomitant increased accumulation of p62 levels suggested that autophagy was induced but its maturation was blocked in matrix-deprived conditions. This block was confirmed by observations of less co-localization of GFP-LC3 and LAMP2, indicating a defect in autophagosome and lysosome fusion. Such blockage can promote rapid exhaustion of energy and accumulation of undigested cargo that can lead to increased anoikis in stressed condition (*27*). This hypothesis is reinforced by recent reports suggesting that induction of autophagy along with blockage of autophagy maturation has adverse effect on cell survival as compared to only blockage of autophagic maturation (*27*).

ERK signaling is often hyper-activated in cancers, leading to uncontrolled growth (*44*). However, accumulating evidence also suggests that its sustained activation may promote apoptosis (*45*). In lung carcinoma and ovarian cancers, ERK signaling was associated with anoikis resistance (*46, 47*). Several pieces of our data pointed towards elevated ERK signaling in matrix-detached cells compared to adherent cells, based on which we originally hypothesized that elevated ERK signaling contributes to anoikis resistance in breast cancer cells. Interestingly, however, our subsequent data revealed that matrix detachment-triggered AMPK, which we have previously shown to be critical for anoikis resistance (*11, 29*), leads to ERK inhibition and consequent progression through autophagy and cell survival, revealing context-specific anti-tumorigenic functions of ERK signaling. A recent report also suggests

that cells with high ERK activity have more stem cell like property and could form more number of anchorage independent colonies (*48*). Similarly, we recently demonstrated inhibition of Akt, typically a pro-tumorigenic signaling molecule (*49*), confers better survival benefits to matrix-detached cells (*11*). Together, these data begin to unfurl novel context-specific signaling networks that can maintain a pro-survival state of matrix-detached cancer cells, identifying new vulnerabilities.

Diverse upstream stimuli converge on MEK to activate ERK (*44*). In matrix-deprived cells, we did not observe change in MEK activity, the only reported upstream kinase of ERK (*44*), suggesting that the increased activity of ERK in matrix-deprived cells does not involve canonical Ras-Raf-MEK pathway. We previously reported that matrix-deprivation triggered AMPK phosphorylates PEA15 (*29*) - a scaffold protein for ERK that can regulate its activity (*50*). The phosphorylation of PEA15 targets ERK to one of its substrates, RSK2, thus promoting its activity (*51*). In this study, we observed that phosphorylation of PEA15 at S116 residue results in inhibition of ERK possibly through reduced association with MEK. Previous literature using yeast two-hybrid system showed that among other members of the MAPK signaling pathway, only ERK interacts with PEA15 (*52*). Our immunoprecipitation studies revealed presence of MEK in PEA15-pull down complex in matrix-deprived cells. There could be a direct interaction between MEK and PEA15, aided possibly by post-translational modifications under matrix-detachment. Alternatively, this interaction could be indirect via ERK which interacts directly with PEA15 irrespective of the phosphorylation status (*33*). Our data show that PEA15 phosphorylation contributes to cancer cell survival in suspension by inhibiting ERK activity and promoting autophagy maturation.

ERK has been reported to regulate autophagy by restricting the nuclear entry of TFEB - a master regulator of transcription of genes required for lysosomal biogenesis and autophagy (*34*). However, we observed a change in levels, but not in nuclear localization, of TFEB in suspension, a change which was dependent on elevated ERK activity. ERK inhibition did not change the transcript levels of TFEB, but led to its increased stability, suggesting a post-transcriptional control of TFEB by pERK. Interestingly, overexpression of TFEB positively regulated AMPK activity. We further show that increase in ROS levels by TFEB is needed for increase in AMPK activity under matrix deprivation. Previous studies suggest that TFEB promotes lysosome biogenesis and autophagic flux (*34*, *35*). Lysosome is reported as an additional source of ROS along with mitochondria (*53*). Lysosomal ROS production could support mitochondrial ROS burst, resulting in overall increase in ROS levels (*53*). Thus,

TFEB by promoting lysosomal biogenesis might promote ROS production and in turn activation of AMPK. However, further experiments are needed to dissect out this possibility.

We demonstrate that pAMPK and TFEB form a positive feedback loop-involving pERK. This feedback loop can result in heterogeneous subpopulations: those with pAMPK^{high}/pERK^{low}/ TFEB^{high} status and those with pAMPK^{low}/pERK^{high}/TFEB^{low} status. The pAMPK^{high}/pERK^{low}/ TFEB^{high} cells displayed elevated autophagic maturation, less apoptosis, and increased sphere-forming potential compared to pAMPK^{low}/pERK^{high}/TFEB^{low} cells. Consistently, a recent report showed that mammary tumors cells with pERK^{high} status were less tumorigenic when cultured in matrix-deprived condition, as compared to pERK^{low} cells (*48*). Finally, in publicly available RNA-seq data of breast cancer patients (*37*), we observed an elevated AMPK and TFEB signature but lower ERK signature in CTC clusters relative to that in individual CTCs. This observation corroborates with higher aggressiveness and poor prognosis of clusters of CTCs (*37*), and emphasizes a pro-metastatic role of pAMPK^{high}/pERK^{low}/TFEB^{high} state. Collectively, our data suggest that pAMPK^{high}/ pERK^{low}/TFEB^{high} status is favourable for survival under matrix deprivation **(Figure 8F)**.

Mutually activating – such as those between phosphorylated AMPK and TFEB – or mutually inhibiting – such as those operating between phosphorylated AMPK and phosphorylated Akt (*11*) – feedback loops can facilitate phenotypic plasticity among these subpopulations (*10*), thus generating non-genetic heterogeneity (*54*) due to underlying multistability (*55*). Similar feedback loops have been reported to mediate cellular plasticity in cancer cells such as epithelial-mesenchymal plasticity (*56, 57*), switching between a cancer stem cell and a non-cancer stem cell (*58*), metabolic plasticity (*55, 59*), or switching between a matrix-deprived and a matrix-attached condition (*11*). Such dynamic interconversions – driven by multiple forms of 'noise' or stochasticity in biological systems (*60, 61*) may enable a more adaptive cellular stress response. Some feedback loops may also operate across multiple cells, hence affecting these different processes in a non-cell autonomous manner, and giving rise to intriguing spatial patterns of heterogeneity (*62*). Therefore, breaking these feedback loops may severely impair the non-genetic heterogeneity and consequently the fitness of a stressed cellular population.

Acknowledgements

We thank Prof. Wilfried Roth for kindly providing the plasmids pcDNA3-Flag-WT-PEA15 and S116A-PEA15. We would like to acknowledge Dr. Benoit Viollet for AMPK DKO cells, Ms. Tamasa De for help in mouse experiment. This work was majorly supported from Wellcome Trust/DBT India Alliance Fellowship (grant number 500112-Z-09-Z) awarded to A. Rangarajan. MKJ acknowledges Ramanujan Fellowship provided by SERB, DST, Government of India (award number SB/S2/RJN-049/2018). We acknowledge support from DBT's National Women Bioscientist Award (2013) to AR, DBT-IISc partnership program to AR, and DST-FIST and UGC, Government of India, to the Department of MRDG. SK acknowledges Council for Scientific and Industrial Research for CSIR fellowship (18-12/2011 (ii) EU-V). We would like to thank FACS-facilities (IISc and MRDG), and Central animal facility (IISc).. SK acknowledges Council for Scientific and Industrial Research for CSIR fellowship (18-12/2011 (ii) EU-V). We would like to thank FACS-facilities (IISc and MRDG), and Central animal facility (IISc).

Conflict of interest

We wish to confirm that there is no conflict of interest.

Reference

1. S. M. Frisch, H. Francis, Disruption of epithelial cell-matrix interactions induces apoptosis. *The Journal of cell biology* **124**, 619-626 (1994).

2. S. M. Frisch, R. A. Screaton, Anoikis mechanisms. *Current opinion in cell biology* **13**, 555-562 (2001).

3. C. D. Simpson, K. Anyiwe, A. D. Schimmer, Anoikis resistance and tumor metastasis. *Cancer letters* **272**, 177-185 (2008).

4. C. Fung, R. Lock, S. Gao, E. Salas, J. Debnath, Induction of autophagy during extracellular matrix detachment promotes cell survival. *Molecular biology of the cell* **19**, 797-806 (2008).

5. C. He, D. J. Klionsky, Regulation mechanisms and signaling pathways of autophagy. *Annual review of genetics* **43**, (2009).

6. S. Fulda, Autophagy and cell death. *Autophagy* **8**, 1250-1251 (2012).

7. V. Marx. (Nature Publishing Group, 2015).

8. X.-j. Zhang, S. Chen, K.-x. Huang, W.-d. Le, Why should autophagic flux be assessed? *Acta Pharmacologica Sinica* **34**, 595 (2013).

9. A. Avivar-Valderas, E. Salas, E. Bobrovnikova-Marjon, J. A. Diehl, C. Nagi, J. Debnath, J. A. Aguirre-Ghiso, PERK integrates autophagy and oxidative stress responses to promote survival during ECM detachment. *Molecular and cellular biology*, MCB. 05164-05111 (2011).

10. D. Jia, M. K. Jolly, P. Kulkarni, H. Levine, Phenotypic plasticity and cell fate decisions in cancer: insights from dynamical systems theory. *Cancers* **9**, 70 (2017).

11. M. Saha, S. Kumar, S. Bukhari, S. A. Balaji, P. Kumar, S. K. Hindupur, A. Rangarajan, AMPK-AKT double negative feedback loop in breast cancer cells regulates their adaptation to matrix deprivation. *Cancer research*, canres. 2090.2017 (2018).

12. A. Sundararaman, U. Amirtham, A. Rangarajan, Calcium-oxidant signaling network regulates ampk activation upon matrix-deprivation. *Journal of Biological Chemistry*, jbc. M116. 731257 (2016).

13. N. L. Collins, M. J. Reginato, J. K. Paulus, D. C. Sgroi, J. LaBaer, J. S. Brugge, G1/S cell cycle arrest provides anoikis resistance through Erk-mediated Bim suppression. *Molecular and cellular biology* **25**, 5282-5291 (2005).

14. A. R. Grassian, Z. T. Schafer, J. S. Brugge, ErbB2 stabilizes epidermal growth factor receptor (EGFR) expression via Erk and Sprouty2 in extracellular matrix-detached cells. *Journal of Biological Chemistry* **286**, 79-90 (2011).

15. A. Al-Ayoubi, A. Tarcsafalvi, H. Zheng, W. Sakati, S. T. Eblen, ERK activation and nuclear signaling induced by the loss of cell/matrix adhesion stimulates anchorage-independent growth of ovarian cancer cells. *Journal of cellular biochemistry* **105**, 875-884 (2008).

16. S. Varma, J. Voldman, A cell-based sensor of fluid shear stress for microfluidics. *Lab on a Chip* **15**, 1563-1573 (2015).

17. A. Eisenberg-Lerner, S. Bialik, H.-U. Simon, A. Kimchi, Life and death partners: apoptosis, autophagy and the cross-talk between them. *Cell death and differentiation* **16**, 966 (2009).

18. E. Corcelle, N. Djerbi, M. Mari, M. Nebout, C. Fiorini, P. Fénichel, P. Hofman, P. Poujeol, B. Mograbi, Control of the autophagy maturation step by the MAPK ERK and p38: lessons from environmental carcinogens. *Autophagy* **3**, 57-59 (2007).

19. N. Mizushima, T. Yoshimori, How to interpret LC3 immunoblotting. *Autophagy* **3**, 542-545 (2007).

20. X. H. Liang, S. Jackson, M. Seaman, K. Brown, B. Kempkes, H. Hibshoosh, B. Levine, Induction of autophagy and inhibition of tumorigenesis by beclin 1. *Nature* **402**, 672 (1999).

21. S. Pankiv, T. H. Clausen, T. Lamark, A. Brech, J.-A. Bruun, H. Outzen, A. Øvervatn, G. Bjørkøy, T. Johansen, p62/SQSTM1 binds directly to Atg8/LC3 to facilitate degradation of ubiquitinated protein aggregates by autophagy. *Journal of biological chemistry*, (2007).

22. S. R. Yoshii, N. Mizushima, Monitoring and measuring autophagy. *International journal of molecular sciences* **18**, 1865 (2017).

23. E. Tresse, F. A. Salomons, J. Vesa, L. C. Bott, V. Kimonis, T.-P. Yao, N. P. Dantuma, J. P. Taylor, VCP/p97 is essential for maturation of ubiquitin-containing autophagosomes and this function is impaired by mutations that cause IBMPFD. *Autophagy* **6**, 217-227 (2010).

24. K. Castillo, V. Valenzuela, S. Matus, M. Nassif, M. Onate, Y. Fuentealba, G. Encina, T. Irrazabal, G. Parsons, F. Court, Measurement of autophagy flux in the nervous system in vivo. *Cell death & disease* **4**, e917 (2013).

25. E.-L. Eskelinen, A. L. Illert, Y. Tanaka, G. n. Schwarzmann, J. Blanz, K. Von Figura, P. Saftig, Role of LAMP-2 in lysosome biogenesis and autophagy. *Molecular biology of the cell* **13**, 3355-3368 (2002).

26. H. Pi, M. Li, L. Tian, Z. Yang, Z. Yu, Z. Zhou, Enhancing lysosomal biogenesis and autophagic flux by activating the transcription factor EB protects against cadmium-induced neurotoxicity. *Scientific reports* **7**, 43466 (2017).

27. K. Kucharewicz, M. Dudkowska, A. Zawadzka, M. Ogrodnik, A. A. Szczepankiewicz, Z. Czarnocki, E. Sikora, Simultaneous induction and blockade of autophagy by a single agent. *Cell death & disease* **9**, 353 (2018).

28. C. H. Wong, K. B. Iskandar, S. K. Yadav, J. L. Hirpara, T. Loh, S. Pervaiz, Simultaneous induction of non-canonical autophagy and apoptosis in cancer cells by ROS-dependent ERK and JNK activation. *PloS one* **5**, e9996 (2010).

29. S. K. Hindupur, S. A. Balaji, M. Saxena, S. Pandey, G. S. Sravan, N. Heda, M. V. Kumar, G. Mukherjee, D. Dey, A. Rangarajan, Identification of a novel AMPK-PEA15 axis in the anoikis-resistant growth of mammary cells. *Breast Cancer Research* **16**, 420 (2014).

30. T. Ng, G. Leprivier, M. Robertson, C. Chow, M. Martin, K. Laderoute, E. Davicioni, T. Triche, P. Sorensen, The AMPK stress response pathway mediates anoikis resistance through inhibition of mTOR and suppression of protein synthesis. *Cell death and differentiation* **19**, 501 (2012).

31. S. L. Hwang, Y. T. Jeong, X. Li, Y. D. Kim, Y. Lu, Y. C. Chang, I. K. Lee, H. W. Chang, Inhibitory cross-talk between the AMPK and ERK pathways mediates endoplasmic reticulum stress-induced insulin resistance in skeletal muscle. *British journal of pharmacology* **169**, 69-81 (2013).

32. H.-S. Kim, M.-J. Kim, E. J. Kim, Y. Yang, M.-S. Lee, J.-S. Lim, Berberine-induced AMPK activation inhibits the metastatic potential of melanoma cells via reduction of ERK activity and COX-2 protein expression. *Biochemical pharmacology* **83**, 385-394 (2012).

33. E. Formstecher, J. W. Ramos, M. Fauquet, D. A. Calderwood, J.-C. Hsieh, B. Canton, X.-T. Nguyen, J.-V. Barnier, J. Camonis, M. H. Ginsberg, PEA-15 mediates cytoplasmic sequestration of ERK MAP kinase. *Developmental cell* **1**, 239-250 (2001).

34. C. Settembre, C. Di Malta, V. A. Polito, M. G. Arencibia, F. Vetrini, S. Erdin, S. U. Erdin, T. Huynh, D. Medina, P. Colella, TFEB links autophagy to lysosomal biogenesis. *science*, 1204592 (2011).

35. Y. Sha, L. Rao, C. Settembre, A. Ballabio, N. T. Eissa, STUB1 regulates TFEB-induced autophagy–lysosome pathway. *The EMBO Journal* **36**, 2544-2552 (2017).

36. Q. Zhang, S. Bhattacharya, M. E. Andersen, R. B. Conolly, Computational systems biology and dose-response modeling in relation to new directions in toxicity testing. *Journal of Toxicology and Environmental Health, Part B* **13**, 253-276 (2010).

37. N. Aceto, A. Bardia, D. T. Miyamoto, M. C. Donaldson, B. S. Wittner, J. A. Spencer, M. Yu, A. Pely, A. Engstrom, H. Zhu, Circulating tumor cell clusters are oligoclonal precursors of breast cancer metastasis. *Cell* **158**, 1110-1122 (2014).

38. M. D. Brooks, M. L. Burness, M. S. Wicha, Therapeutic implications of cellular heterogeneity and plasticity in breast cancer. *Cell stem cell* **17**, 260-271 (2015).

39. D. A. Lawson, K. Kessenbrock, R. T. Davis, N. Pervolarakis, Z. Werb, Tumour heterogeneity and metastasis at single-cell resolution. *Nature cell biology* **20**, 1349 (2018).

40. M. L. Suvà, I. Tirosh, Single-Cell RNA Sequencing in Cancer: Lessons Learned and Emerging Challenges. *Molecular cell* **75**, 7-12 (2019).

41. X. Qu, J. Yu, G. Bhagat, N. Furuya, H. Hibshoosh, A. Troxel, J. Rosen, E.-L. Eskelinen, N. Mizushima, Y. Ohsumi, Promotion of tumorigenesis by heterozygous disruption of the beclin 1 autophagy gene. *The Journal of clinical investigation* **112**, 1809-1820 (2003).

42. A. Takamura, M. Komatsu, T. Hara, A. Sakamoto, C. Kishi, S. Waguri, Y. Eishi, O. Hino, K. Tanaka, N. Mizushima, Autophagy-deficient mice develop multiple liver tumors. *Genes & development* **25**, 795-800 (2011).

43. J. Y. Guo, B. Xia, E. White, Autophagy-mediated tumor promotion. *Cell* **155**, 1216-1219 (2013).

44. Y. D. Shaul, R. Seger, The MEK/ERK cascade: from signaling specificity to diverse functions. *Biochimica et Biophysica Acta (BBA)-Molecular Cell Research* **1773**, 1213-1226 (2007).

45. Y. Sun, W.-Z. Liu, T. Liu, X. Feng, N. Yang, H.-F. Zhou, Signaling pathway of MAPK/ERK in cell proliferation, differentiation, migration, senescence and apoptosis. *Journal of Receptors and Signal Transduction* **35**, 600-604 (2015).

46. S. Yoshino, T. Hara, H. J. Nakaoka, A. Kanamori, Y. Murakami, M. Seiki, T. Sakamoto, The ERK signaling target RNF126 regulates anoikis resistance in cancer cells by changing the mitochondrial metabolic flux. *Cell discovery* **2**, 16019 (2016).

47. L. Carduner, C. R. Picot, J. Leroy-Dudal, L. Blay, S. Kellouche, F. Carreiras, Cell cycle arrest or survival signaling through αv integrins, activation of PKC and ERK1/2 lead to anoikis resistance of ovarian cancer spheroids. *Experimental cell research* **320**, 329-342 (2014).

48. Y. Kumagai, H. Naoki, E. Nakasyo, Y. Kamioka, E. Kiyokawa, M. Matsuda, Heterogeneity in ERK activity as visualized by in vivo FRET imaging of mammary tumor cells developed in MMTV-Neu mice. *Oncogene* **34**, 1051 (2015).

49. M. A. Davies, Regulation, role, and targeting of Akt in cancer. *Journal of Clinical Oncology* **29**, 4715-4717 (2011).

50. W. Kolch, Coordinating ERK/MAPK signalling through scaffolds and inhibitors. *Nature reviews Molecular cell biology* **6**, 827 (2005).

51. H. Vaidyanathan, J. Opoku-Ansah, S. Pastorino, H. Renganathan, M. L. Matter, J. W. Ramos, ERK MAP kinase is targeted to RSK2 by the phosphoprotein PEA-15. *Proceedings of the National Academy of Sciences* **104**, 19837-19842 (2007).

52. J. W. Ramos, P. E. Hughes, M. W. Renshaw, M. A. Schwartz, E. Formstecher, H. Chneiweiss, M. H. Ginsberg, Death effector domain protein PEA-15 potentiates Ras activation of extracellular signal receptor-activated kinase by an adhesion-independent mechanism. *Molecular biology of the cell* **11**, 2863-2872 (2000).

53. C. Kubota, S. Torii, N. Hou, N. Saito, Y. Yoshimoto, H. Imai, T. Takeuchi, Constitutive reactive oxygen species generation from autophagosome/lysosome in neuronal oxidative toxicity. *Journal of Biological Chemistry* **285**, 667-674 (2010).

54. M. K. Jolly, P. Kulkarni, K. Weninger, J. Orban, H. Levine, Phenotypic Plasticity, Bet-Hedging, and Androgen Independence in Prostate Cancer: Role of Non-Genetic Heterogeneity. *Frontiers in oncology* **8**, 50 (2018).

55. E. A. Sobie, Bistability in biochemical signaling models. *Sci. Signal.* **4**, tr10-tr10 (2011).

56. M. Lu, M. K. Jolly, H. Levine, J. N. Onuchic, E. Ben-Jacob, MicroRNA-based regulation of epithelial–hybrid–mesenchymal fate determination. *Proceedings of the National Academy of Sciences*, 201318192 (2013).

57. D. Jia, M. K. Jolly, S. C. Tripathi, P. Den Hollander, B. Huang, M. Lu, M. Celiktas, E. Ramirez-Peña, E. Ben-Jacob, J. N. Onuchic, Distinguishing mechanisms underlying EMT tristability. *Cancer convergence* **1**, 2 (2017).

58. M. K. Jolly, B. Huang, M. Lu, S. A. Mani, H. Levine, E. Ben-Jacob, Towards elucidating the connection between epithelial–mesenchymal transitions and stemness. *Journal of The Royal Society Interface* **11**, 20140962 (2014).

59. D. Jia, M. Lu, K. H. Jung, J. H. Park, L. Yu, J. N. Onuchic, B. A. Kaipparettu, H. Levine, Elucidating cancer metabolic plasticity by coupling gene regulation with metabolic pathways. *Proceedings of the National Academy of Sciences* **116**, 3909-3918 (2019).

60. S. M. Mooney, M. K. Jolly, H. Levine, P. Kulkarni, Phenotypic plasticity in prostate cancer: role of intrinsically disordered proteins. *Asian journal of andrology* **18**, 704 (2016).

61. G. Balázsi, A. van Oudenaarden, J. J. Collins, Cellular decision making and biological noise: from microbes to mammals. *Cell* **144**, 910-925 (2011).

62. F. Bocci, L. Gearhart-Serna, M. Boareto, M. Ribeiro, E. Ben-Jacob, G. R. Devi, H. Levine, J. N. Onuchic, M. K. Jolly, Toward understanding cancer stem cell heterogeneity in the tumor microenvironment. *Proceedings of the National Academy of Sciences* **116**, 148-157 (2019).

Figure legends:

Figure 1.

Heterogeneity in ERK activity in matrix-deprived condition

A & B). Comparative analysis of gene expression for microarray data of MDA-MB-231 cells cultured in suspension (Sus) versus attached (Att) conditions for 24 hours:

(A). Heat map of semi-supervised clustering of ERK pathway signature genes. Red represents highly expressed genes, while green represents downregulated genes.

(B). Gene Set Enrichment Analysis (GSEA) plot for ERK pathway.

C & D). MDA-MB-231 cells were cultured in attached (Att) or suspension (Sus) conditions for 24 hours and harvested for immunoblotting (C) and qRT-PCR (D); n=3.

E. Graph represents MDA-MB-231 cells stably expressing $EGR1_{(promoter)}$-TurboRFP cultured in attached (Att) and suspension (Sus) conditions for 24 hours and harvested for analysis of RFP intensity by flow cytometry; n=3.

F. Immunoblot analysis of BT-474 cells cultured in attached (Att), suspension condition (Sus) or anchorage independent cancer spheres (CS) in methylcellulose for 7-days; n=3.

G. Fluorescent images of MDA-MB-231 cells cultured in attached (Att) or suspension (Sus) condition for 24 hours, probed for pERK, and visualized by confocal microscopy (Z-stack, scale bar, 20µM); n=3. Heat map was generated with the help of ImageJ.

H-K). MDA-MB-231 cells stably expressing $EGR1_{(promoter)}$-TurboRFP were cultured in attached (Att) or suspension (Sus) condition for 24 hours and imaged (H). High and low RFP

subpopulations were separated by FACS sorting (I.a) and harvested for immunoblotting (I.b); n=3, caspase-3 activity assay (J); n=3, and anchorage independent colonies formation (K); n=3.

Figure 2.

Matrix deprivation leads to heterogeneity in autophagy maturation.

A. Immunoblot analysis of MDA-MB-231 cells cultured in attached (Att) or suspension (Sus) conditions for 24 hours. Graphs represent densitometric quantification of immunoblots; error bars, mean±SEM; n=3.

B. Fluorescent images of MDA-MB-231 cells stably expressing mCherry-EGFP-LC3 (B) and cultured in attached (Att) condition with or without rapamycin (Rapa), or in suspension (Sus) condition for 24 hours and visualized with confocal microscopy (Z-stack, scale bar, 20μM); n=3. Graph represents ratio of mChrrey/EGFP intensity.

C. Immunofluorescence of MDA-MB-231 cells with anti-p62 antibody cultured in suspension (Sus) condition for 24 hours; n=3. Heat map was generated with the help of ImageJ.

D. Immunofluorescence of MDA-MB-231 cells with anti-LAMP2 antibody (Cy3) and co-localization with GFP-LC3 puncta in cells cultured in suspension (Sus) conditions for 24 hours and visualized with confocal microscopy (Z-stack, scale bar, 10 μM); n=3. Colocalization of LAMP2 and LC3 was measured by Pearson's correlation coefficient employing Coloc-2 plugin in ImageJ and represented as dot plot (each dot represents single cell) (left) as well as bar graph (% of cells with Pearson's correlation </=0.5 in black and >0.5 in gray) (right).

E. Immunofluorescence of MDA-MB-231 cells with anti-cleaved-caspase-3 or anti-p62 antibody cultured in suspension (Sus) condition for 24 hours (yellow arrow represents less cleaved caspase-3^{less}/$p62^{less}$ and white arrow represents cleaved caspase 3^{high}/$p62^{high}$ level) . Heat map was generated with the help of Image J. Spearman correlation analysis between cleaved-caspase-3 and p62 was plotted using excel.

F. MDA-MB-231 cells stably expressing $EGR1_{(promoter)}$-TurboRFP were cultured in suspension (Sus) condition for 24 hours. High and low RFP subpopulations were separated by FACS sorting and harvested for immunoblotting (H); n=3.

G. Immunofluorescence of MDA-MB-231 cells stably expressing $EGR1_{(promoter)}$-TurboRFP with anti-p62 antibody cultured in suspension (Sus) condition for 24 hours (yellow arrow represents $RFP^{less}/p62^{less}$ and white arrow represents $RFP^{high}/p62^{high}$). Heat map was generated with the help of ImageJ. Spearman correlation analysis between p62 and TurboRFP was plotted using excel.

Figure 3.

Inhibition of ERK signaling promotes autophagy maturation and alleviates apoptosis in matrix-deprived condition

A. Immunoblot analysis of MDA-MB-231 cells cultured in suspension (Sus) condition for 24 hours in presence of vehicle control (DMSO) or MEK-inhibitor (PD98059); n=3.

B. Immunoblot analysis of MCF-7 cells transiently transfected with empty vector or MEK-K101A were cultured in suspension (Sus) condition for 24 hours; n=2.

C. Fluorescence images of MDA-MB-231 cells stably expressing mCherry-EGFP-LC3 construct cultured in suspension (Sus) condition for 24 hours in presence of DMSO or PD98059 and visualized with confocal microscopy (Z-stack, scale bar, 10 µM); n=3. Graph represents ratio of mChrrey/EGFP intensity.

D. Immunofluorescence of MDA-MB-231 cells with anti-LAMP2 antibody (Cy3) and co-localization with GFP-LC3 puncta in cells cultured in suspension (Sus) condition for 24 hours in presence of DMSO or PD98059 and visualized with confocal microscopy (Z-stack, scale bar, 10 µM); n=3. Colocalization of LAMP2 and LC3 was measured by Person's correlation coefficient employing Coloc-2 plugin in ImageJ and represented as dot plot (each dot represents single cell) (left) as well as bar graph (% of cells with Pearson's correlation </=0.5 in black and >0.5 in gray) (right).

E. Graph represents densitometric quantification of immunoblots for BT-474 cells grown in suspension (Sus) condition for 24 hours in the presence of DMSO or PD98059 (also see **Figure S3C**); n=3.

F. Flow cytometric analysis of caspase-3 activity of MDA-MB-231 cells cultured in attached (Att) or suspension (Sus) conditions for 24 hours in presence of DMSO or PD98059 ; n=3.

G. Representative images of lung metastasis following intraperitoneal injection of EAC cells after culturing in suspension (Sus) condition in presence of DMSO or PD98059. Black

arrows depict macrometastatic nodules (a). Black circles indicates the presence of a micro metastatic lesion in histological sections (10× magnification) (b); n=3.

Figure 4.

AMPK inhibits ERK activity in suspension and promotes autophagy maturation

A. MDA-MB-231 cells stably expressing $EGR1_{(promoter)}$-TurboRFP were cultured in suspension (Sus) condition for 24 hours. High and low RFP subpopulations were separated by FACS sorting and harvested for immunoblotting; n=3.

B. Immunofluorescence of MDA-MB-231 cells with anti-pACC or anti-pERK antibody cultured in suspension (Sus) condition for 24 hours (yellow arrow represents $pACC^{low}/pERK^{high}$ and white arrow represents $pACC^{high}/pERK^{low}$); n=2. Scatter and co-relation graph was plotted using excel. Spearman correlation analysis between pACC and pERK was plotted using excel.

C. Immunofluorescence of lactating mammary glands of mouse for anti-pAMPK and anti-pERK and visualised with confocal microscopy (Z-stack, scale bar, 40 µM); n=3.

D & E). Representative immunoblots of following cell lysates were probed for specified proteins:

(D) BT-474 cells cultured in suspension (Sus) condition for 24 hours in presence of vehicle control (DMSO) or AMPK inhibitor (compound C); n=5.

(E). Wild type mouse embryonic fibroblast (WT-MEF) or double knock out for AMPKα1/α2 (AMPK DKO) cultured in suspension (Sus) condition for 24 hours; n=3.

F. MDA-MB-231 cells were cultured in attached (Att) or suspension (Sus) conditions for 24 hours in presence of vehicle control (DMSO), MEK-inhibitor (PD98059) or AMPK inhibitor (compound C) followed by qRT-PCR analysis for the indicated gene; n=3.

G. MDA-MB-231 cells stably expressing $EGR1_{(promoter)}$-TurboRFP were cultured in suspension (Sus) condition for 24 hours in presence of vehicle control (DMSO), MEK-inhibitor (PD98059) or AMPK inhibitor (compound C) for 24 hours and harvested for analysis of RFP intensity by flow cytometry; n=3.

H. Dot plot (left) and bar graphs (right) showing Pearson's coefficient (% of cells with Pearson's correlation </=0.5 in black and >0.5 in gray) as a measure of colocalization of LAMP2 and GFP-LC3 in MDA-MB-231 cells cultured in suspension (Sus) condition for 24 hours in presence of vehicle control (DMSO) or AMPK inhibitor (compound C) with or without MEK-inhibitor (PD98059) (also see **Figure S4C**); n=3.

I. Flow cytometric analysis of caspase-3 activity for MDA-MB-231 cells cultured in suspension (Sus) condition for 24 hours in presence of vehicle control (DMSO), MEK-inhibitor (PD98059), AMPK inhibitor (compound C) with or without MEK-inhibitor (PD98059) for 24 hours; n=3.

Figure 5.

AMPK negatively regulates MEK-mediated activation of ERK by phosphorylation of PEA15

A & B). Immunoblots analysis of following cell lysates were harvested and probed for specified proteins:

(A). MDA-MB-231 cells stably expressing $EGR1_{(promoter)}$-TurboRFP were cultured in suspension (Sus) condition for 24 hours. High and low RFP subpopulations were separated by FACS sorting; n=3.

(B). MDA-MB-231 cells stably overexpressing Flag-tag wild type PEA15 (WT-PEA15) or nonphosphorylatable mutant of PEA15 (S116A-PEA15) cultured in suspension (Sus) condition for 24 hours; n=5.

C & D). Immunoblots analysis of immunoprecipitated (IP) products with IgG control or anti-Flag antibodies of cell lysates harvested in following conditions. 2% of the whole-cell lysate was used as input and probed for specified proteins:

(C). MCF-7 cells transiently transfected with Flag-tag-WT-PEA15 cultured in the suspension (Sus) condition for 24 hours; n=3.

(D). MCF-7 cells transiently transfected with Flag-tag-WT-PEA15 cultured in the suspension (Sus) condition for 24 hours; n=3.

E. Immunoblots analysis of MCF-7 cells cultured in suspension condition (Sus) for 24 hours after transfection with siControl or siPEA15; n=3.

F. Immunoblot analysis of immunoprecipitated (IP) products with IgG control or anti-tPEA15 antibodies from MDA-MB-231 cells cultured in suspension (Sus) condition for 24 hours in presence of vehicle control (DMSO) or AMPK inhibitor (compound C). 2% of the whole-cell lysate was used as input and probed for specified proteins; n=3.

G. Immunoblots analysis of MDA-MB-231 cells stably overexpressing Flag-tag WT-PEA15 or S116A-PEA15 cultured in suspension (Sus) condition in presence of vehicle control (DMSO) or MEK-inhibitor (PD98059); n=3.

H. Dot plot (left) and bar graphs (right) showing Pearson's coefficient (% of cells with Pearson's correlation coefficient </=0.5 in black and >0.5 in gray) as a measure of colocalization of LAMP2 and GFP-LC3 MDA-MB-231 cells stably overexpressing wild type PEA15 (WT-PEA15) or nonphosphorylatable mutant of PEA15 (S116A-PEA15) treated with vehicle control (DMSO) or MEK-inhibitor (PD98059) and cultured in suspension (Sus) condition for 24 hours (also see **Figure S5H**); n=3.

Figure 6.

AMPK upregulates TFEB level by inhibition of ERK activity in matrix-deprived condition

A-D). Immunoblots of following cell lysates were harvested and probed for specified proteins:

(A). MDA-MB-231 cells stably expressing $EGR1_{(promoter)}$-TurboRFP were cultured in suspension (Sus) condition for 24 hours. High and low RFP subpopulations were separated by FACS sorting; n=3.

(B). MDA-MB-231 cells cultured in suspension (Sus) for 24 hours in presence of vehicle control (DMSO) or MEK-inhibitor (PD98059); n=3.

(C). MDA-MB-231 cells cultured in suspension for 24 hours in presence of vehicle control (DMSO) or AMPK inhibitor (CC); n=3.

(D). MDA-MB-231 cells cultured in suspension for 24 hours in presence of AMPK inhibitor (compound C) plus treated with vehicle control (DMSO) or MEK-inhibitor (PD98059); n=3.

E. Graph represents mean fluorescence intensity of LAMP2 (Cy5) in MDA-MB-231 cells stably expressing control empty vector or EGFP-tagged TFEB cultured in suspension

condition for 24 hours (≥50 cells analysed per sample/experiment) (also see **Figure S6H**); n=3.

F. Dot plot (left) and bar graphs (right) showing Pearson's coefficient (% of cells with Pearson's correlation coefficient </=0.5 in black and >0.5 in gray) as a measure of colocalization of LAMP2 and RFP-LC3 in MDA-MB-231 cells stably overexpressing control empty vector or EGFP-TFEB were cultured in suspension (Sus) condition for 24 hours in presence of vehicle control (DMSO) or AMPK inhibitor (CC) (also see **Figure S6I**); n=3.

G. Graph represents mean fluorescence intensity of LAMP2 in MDA-MB-231 cells stably overexpressing control empty vector or EGFP-TFEB cultured in suspension (Sus) condition for 24 hours in presence of vehicle control (DMSO) or AMPK inhibitor (compound C) (≥50 cells analysed per sample/experiment) (also see **Figure S6J**); n=5.

H & I). MDA-MB-231 cells stably expressing control empty vector and EGFP tagged TFEB cultured in suspension (Sus) condition for 24 hours in presence of vehicle control (DMSO) or AMPK inhibitor (compound C) and harvested for flow cytometric analysis of caspase-3 activity (H) and anchorage independent colonies formation (I); n=2.

Figure 7.

TFEB-mediated upregulation of AMPK activity

A. Immunoblot analysis of MDA-MB-231 cells stably overexpressing control empty vector (EV) or EGFP-TFEB were cultured in suspension (Sus) condition for 24 hours; n=3.

B. Graph represent mean fluorescence intensity of pACC (Cy3) in MDA-MB-231 cells stably overexpressing control empty vector or EGFP tagged TFEB cultured in suspension (Sus) condition for 24 hours (≥50 cells analysed per sample/experiment) (also see **Figure S7A**); n=3.

C & D). MDA-MB-231 cells stably overexpressing Scr control or shTFEB#C5 cultured in suspension (Sus) condition for 24 hours and harvested for immunoblotting (C) and immunocytochemistry (ICC) (D) (also see **Figure S7D**); n=3.

E. Dot plot (left) and bar graphs (right) showing Pearson's coefficient (% of cells with Pearson's correlation coefficient </=0.5 in black and >0.5 in gray) as a measure of colocalization of GFP-LC3 and LAMP2 in MDA-MB-231 cells stably overexpressing Scr

control or shTFEB#C5 cultured in suspension (Sus) condition for 24 hours (also see **Figure S7E**); n=3.

F. Immunoblot analysis of MDA-MB-231 cells stably overexpressing EGFP-TFEB were cultured in suspension (Sus) condition for 24 hours in presence of vehicle control or N-acetyl-L-cysteine (NAC); n=2.

G. Immunoblots analysis of MDA-MB-231 cultured in suspension (Sus) condition for 24 hours in presence of vehicle control (DMSO) or MEK-inhibitor (PD98059) for 24 hours; n=3.

H. Graph represent mean fluorescence intensity of pACC (Cy3) in MDA-MB-231 cells cultured in suspension (Sus) condition for 24 hours in presence of vehicle control (DMSO) or MEK-inhibitor (PD98059) ($\geq$50 cells analysed per sample/experiment) (also see **Figure S7H**); n=3.

Figure 8

Feedback loop between AMPK and TFEB via PEA15-ERK confers autophagy maturation and anoikis resistance

A. Potential feedback loops that can represent possible cross talk between AMPK, ERK, and TFEB in matrix-deprived condition.

B. Immunoblot analysis of MDA-MB-231 cells stably overexpressing control empty vector or EGFP-TFEB were cultured in suspension (Sus) condition for 24 hours in presence of vehicle control (DMSO) or AMPK-inhibitor (CC) for 24 hours; n=3.

C. (left) Nullclines generated by the mathematical model for network II; they represent the change of steady state concentration of pAMPK with change in TFEB concentration (blue) and vice versa (red). The intersections of the two curves represent the steady states of the system. Intersections highlighted in green are stable steady states, i.e., cellular phenotypes, while that highlighted in white represents the “tipping point” for transitions among these phenotypes. (right) Stochastic variations can lead to cells dynamically switching among the two phenotypes upon various perturbations, once they cross the tipping point (highlighted by red line).

D. MDA-MB-231 cells stably expressing $EGR1_{(promoter)}$-TurboRFP were cultured in suspension (Sus) condition for 24 hours. High and low RFP subpopulations were FACS

sorting and cultured in suspension condition (Sus) and analysed at the indicated time points; n=3.

E. Box plots show distribution of expression of ERK, AMPK, or TFEB-dependent genes from RNA-sequencing data publicly available for 15 single CTCs pools and matched 14 CTC clusters isolated from ten breast cancer patients (SC, single CTCs; CL, CTC cluster) (GSE51827) (also see **Figure S8E and S8F**).

F. **Model:** Matrix-deprivation triggered AMPK inhibits ERK activity through phosphorylation of PEA15. Phosphorylation of PEA15 leads to inhibition of ERK activity, which results in increased TFEB level. Increased TFEB promotes autophagy maturation as well as AMPK activity. TFEB mediated upregulation of AMPK activity can enhance the inhibitory effect on ERK, resulting in increased autophagy maturation and, in turn, better cell survival in suspension.

Figure 1

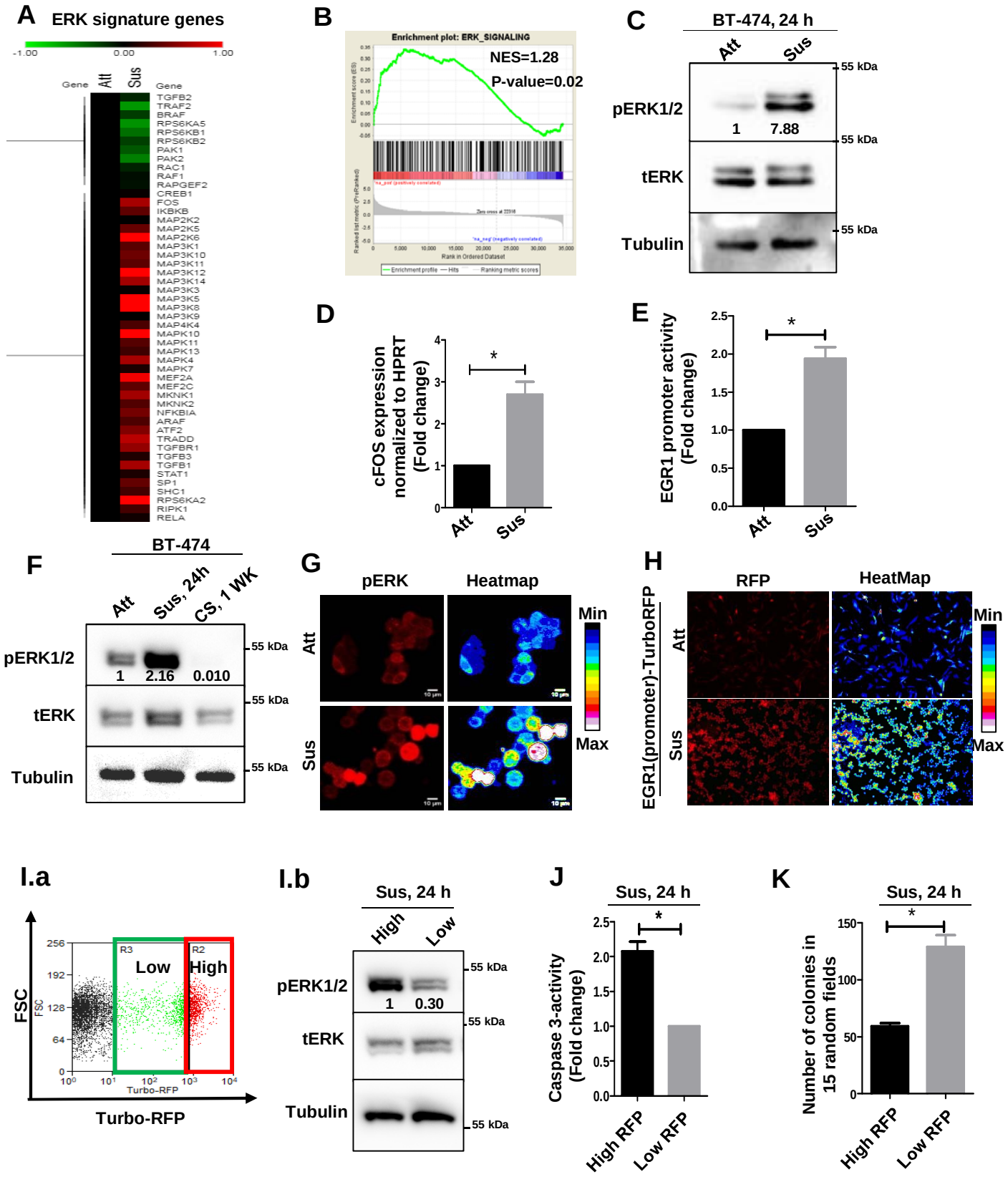
A
ERK signature genes
-1.00
0.00
1.00
Gene
Att
Sus
Gene
TGFB2
TRAF2
BRAF
RPS6KA5
RPS6KB1
RPS6KB2
PAK1
PAK2
RAC1
RAF1
RAPGEF2
CREB1
FOS
IKBKB
MAP2K2
MAP2K5
MAP2K6
MAP3K1
MAP3K10
MAP3K11
MAP3K12
MAP3K14
MAP3K3
MAP3K5
MAP3K8
MAP3K9
MAP4K4
MAPK10
MAPK11
MAPK13
MAPK4
MAPK7
MEF2A
MEF2C
MKNK1
MKNK2
NFKBIA
ARAF
ATF2
TRADD
TGFBR1
TGFB3
TGFB1
STAT1
SP1
SHC1
RPS6KA2
RIPK1
RELA
B
Enrichment plot: ERK_SIGNALING
NES=1.28
P-value=0.02
Rank in Ordered Dataset
C
BT-474, 24 h
Att
Sus
pERK1/2
1
7.88
tERK
Tubulin
55 kDa
D
cFOS expression normalized to HPRT (Fold change)
Att
Sus
E
EGR1 promoter activity (Fold change)
Att
Sus
F
BT-474
Att
Sus, 24h
CS, 1 WK
pERK1/2
1
2.16
0.010
tERK
Tubulin
55 kDa
G
pERK
Heatmap
Att
Sus
Min
Max
H
RFP
HeatMap
EGR1(promoter)-TurboRFP
Att
Sus
Min
Max
I.a
FSC
Turbo-RFP
R3
Low
R2
High
I.b
Sus, 24 h
High
Low
pERK1/2
1
0.30
tERK
Tubulin
55 kDa
J
Sus, 24 h
Caspase 3-activity (Fold change)
High RFP
Low RFP
K
Sus, 24 h
Number of colonies in 15 random fields
High RFP
Low RFP

Figure 2

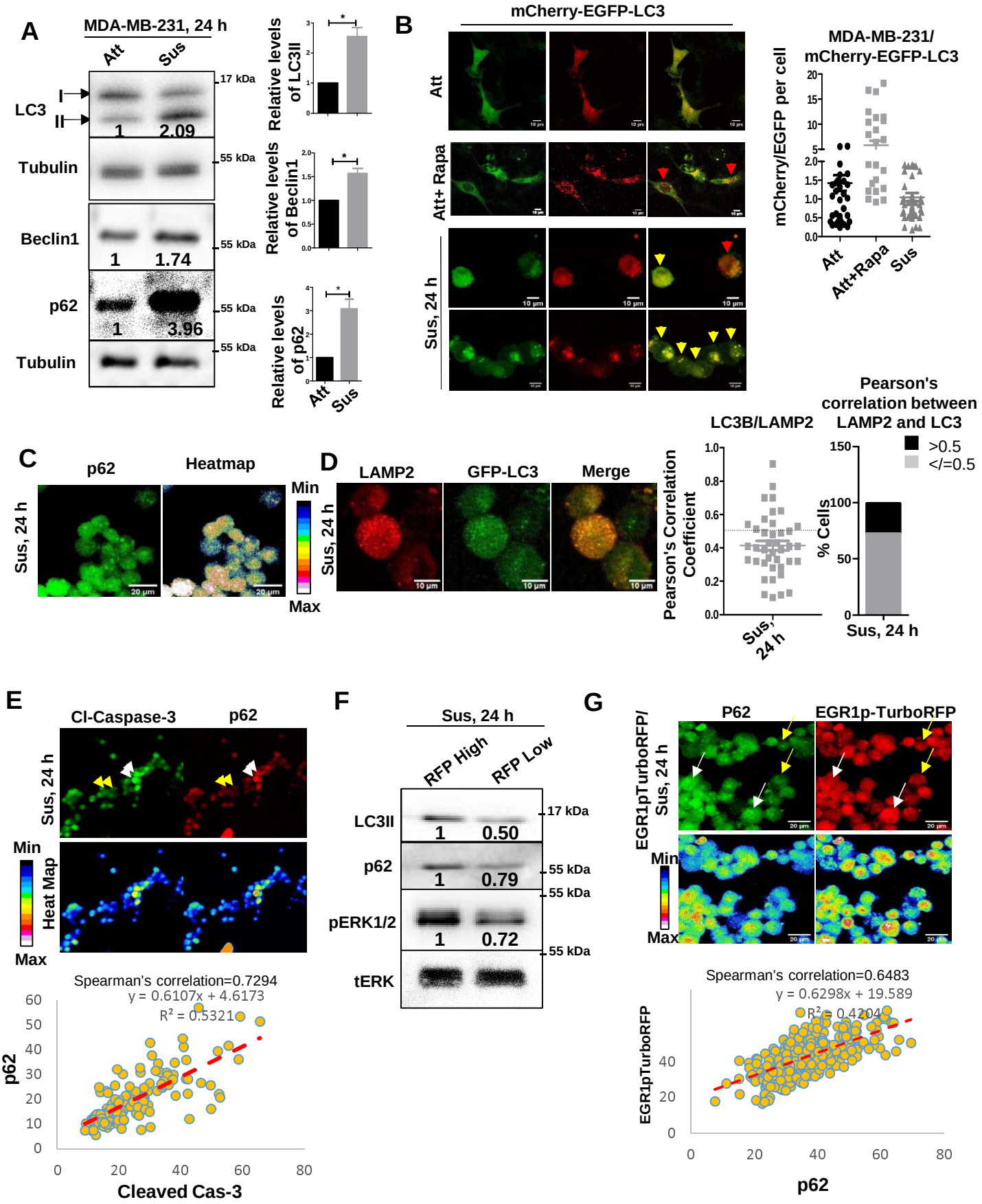
A
MDA-MB-231, 24 h
Att
Sus
LC3
I
II
17 kDa
1
2.09
Tubulin
55 kDa
Beclin1
1
1.74
p62
1
3.96
Tubulin
Relative levels of LC3II
Relative levels of Beclin1
Relative levels of p62
B
mCherry-EGFP-LC3
Att
Att+ Rapa
Sus, 24 h
MDA-MB-231/ mCherry-EGFP-LC3
mCherry/EGFP per cell
C
p62
Heatmap
Sus, 24 h
Min
Max
D
LAMP2
GFP-LC3
Merge
Sus, 24 h
LC3B/LAMP2
Pearson's Correlation Coefficient
Pearson's correlation between LAMP2 and LC3
% Cells
>0.5
</=0.5
Sus, 24 h
E
Cl-Caspase-3
p62
Sus, 24 h
Min
Heat Map
Max
Spearman's correlation=0.7294
y = 0.6107x + 4.6173
R² = 0.5321
p62
Cleaved Cas-3
F
Sus, 24 h
RFP High
RFP Low
LC3II
1
0.50
p62
1
0.79
pERK1/2
1
0.72
tERK
17 kDa
55 kDa
55 kDa
55 kDa
G
P62
EGR1p-TurboRFP
EGR1pTurboRFP/ Sus, 24 h
Min
Max
Spearman's correlation=0.6483
y = 0.6298x + 19.589
R² = 0.4204
EGR1pTurboRFP
p62

Figure 3

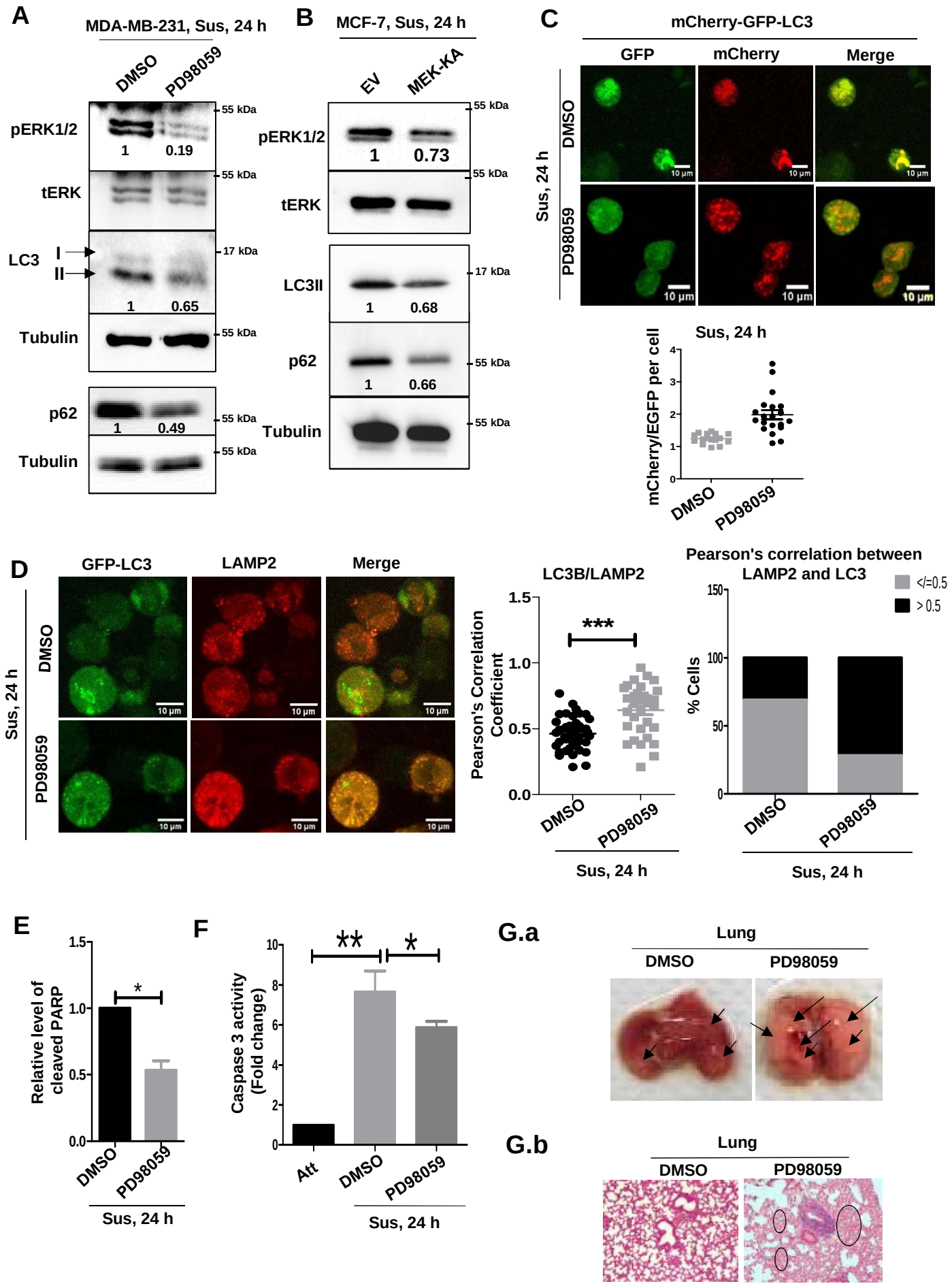
A
MDA-MB-231, Sus, 24 h
DMSO
PD98059
pERK1/2
1
0.19
55 kDa
tERK
55 kDa
LC3
I
II
17 kDa
1
0.65
Tubulin
55 kDa
p62
1
0.49
55 kDa
Tubulin
55 kDa
B
MCF-7, Sus, 24 h
EV
MEK-KA
pERK1/2
1
0.73
55 kDa
tERK
55 kDa
LC3II
17 kDa
1
0.68
p62
1
0.66
55 kDa
Tubulin
55 kDa
C
mCherry-GFP-LC3
GFP
mCherry
Merge
Sus, 24 h
DMSO
PD98059
10 µm
Sus, 24 h
mCherry/EGFP per cell
DMSO
PD98059
D
GFP-LC3
LAMP2
Merge
Sus, 24 h
DMSO
PD98059
10 µm
LC3B/LAMP2
Pearson's Correlation Coefficient
***
DMSO
PD98059
Sus, 24 h
Pearson's correlation between LAMP2 and LC3
</=0.5
> 0.5
% Cells
DMSO
PD98059
Sus, 24 h
E
Relative level of cleaved PARP
*
DMSO
PD98059
Sus, 24 h
F
Caspase 3 activity (Fold change)
**
*
Att
DMSO
PD98059
Sus, 24 h
G.a
Lung
DMSO
PD98059
G.b
Lung
DMSO
PD98059

Figure 4

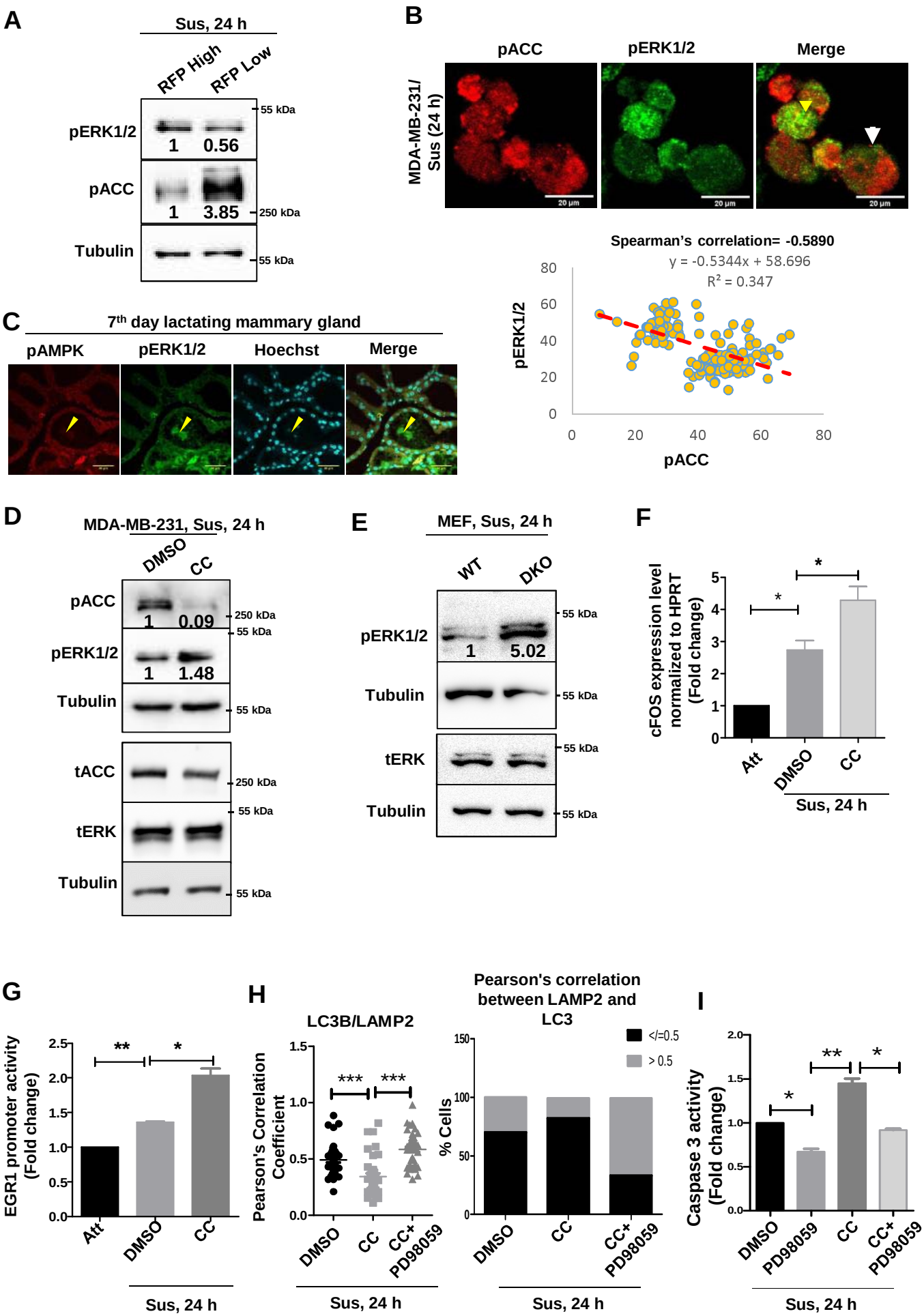
A
Sus, 24 h
RFP High
RFP Low
pERK1/2
1
0.56
55 kDa
pACC
1
3.85
250 kDa
Tubulin
55 kDa
B
pACC
pERK1/2
Merge
MDA-MB-231/ Sus (24 h)
20 µm
Spearman's correlation= -0.5890
y = -0.5344x + 58.696
R² = 0.347
pERK1/2
pACC
C
7th day lactating mammary gland
pAMPK
pERK1/2
Hoechst
Merge
D
MDA-MB-231, Sus, 24 h
DMSO
CC
pACC
1
0.09
250 kDa
55 kDa
pERK1/2
1
1.48
Tubulin
55 kDa
tACC
250 kDa
tERK
55 kDa
Tubulin
55 kDa
E
MEF, Sus, 24 h
WT
DKO
pERK1/2
1
5.02
55 kDa
Tubulin
55 kDa
tERK
55 kDa
Tubulin
55 kDa
F
cFOS expression level normalized to HPRT (Fold change)
Att
DMSO
CC
Sus, 24 h
G
EGR1 promoter activity (Fold change)
Att
DMSO
CC
Sus, 24 h
H
LC3B/LAMP2
Pearson's Correlation Coefficient
DMSO
CC
CC+ PD98059
Sus, 24 h
Pearson's correlation between LAMP2 and LC3
<=0.5
> 0.5
% Cells
DMSO
CC
CC+ PD98059
Sus, 24 h
I
Caspase 3 activity (Fold change)
DMSO
PD98059
CC
CC+ PD98059
Sus, 24 h

Figure 5

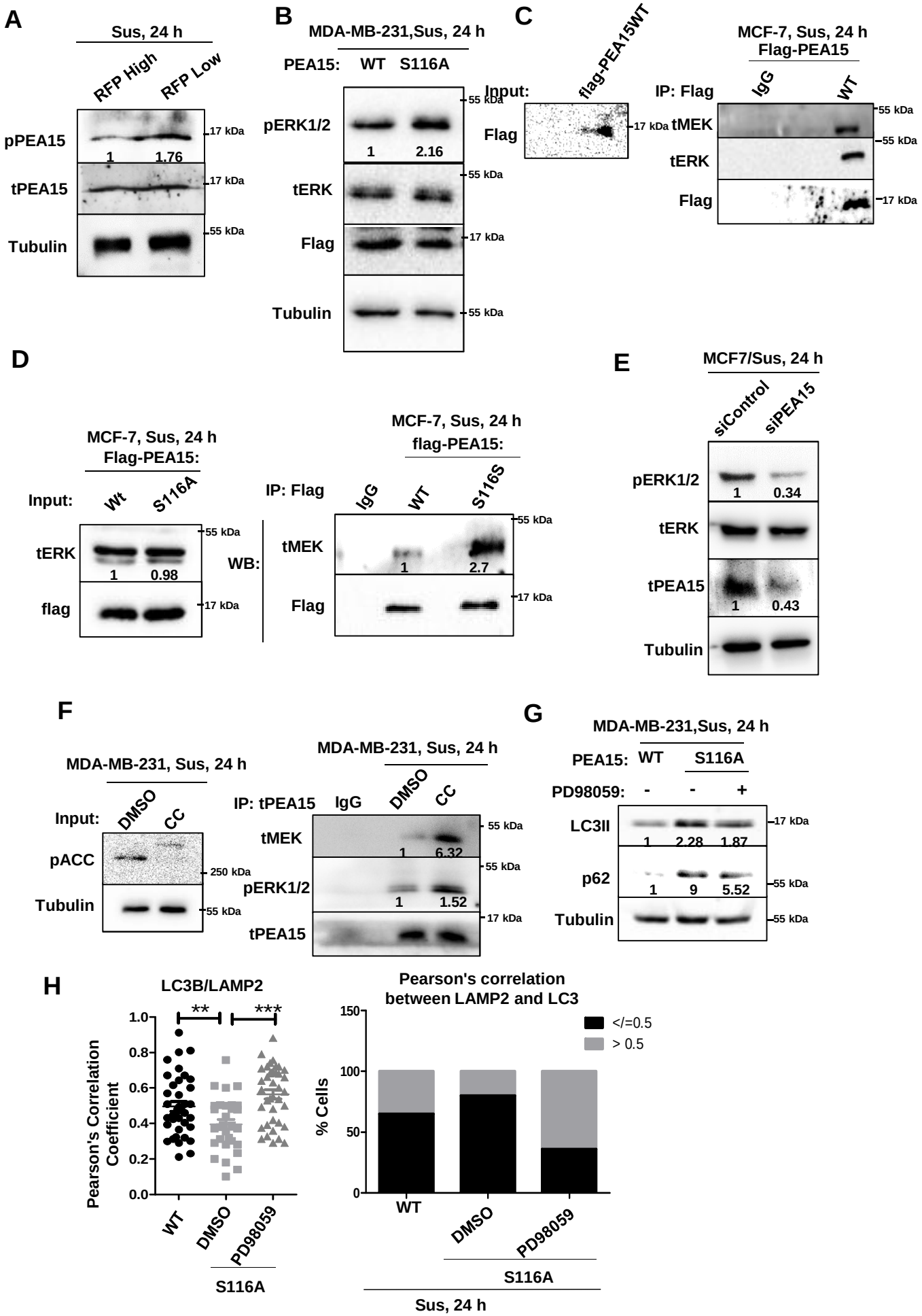
A
Sus, 24 h
RFP High
RFP Low
pPEA15
tPEA15
Tubulin
17 kDa
55 kDa
1
1.76
B
MDA-MB-231,Sus, 24 h
PEA15: WT S116A
pERK1/2
tERK
Flag
Tubulin
1
2.16
C
Input:
flag-PEA15WT
Flag
MCF-7, Sus, 24 h
Flag-PEA15
IP: Flag
IgG
WT
tMEK
tERK
Flag
D
MCF-7, Sus, 24 h
Flag-PEA15:
Input:
Wt
S116A
tERK
flag
1
0.98
WB:
MCF-7, Sus, 24 h
flag-PEA15:
IP: Flag
IgG
WT
S116S
tMEK
Flag
1
2.7
E
MCF7/Sus, 24 h
siControl
siPEA15
pERK1/2
tERK
tPEA15
Tubulin
1
0.34
1
0.43
F
MDA-MB-231, Sus, 24 h
Input:
DMSO
CC
pACC
Tubulin
250 kDa
MDA-MB-231, Sus, 24 h
IP: tPEA15
IgG
DMSO
CC
tMEK
pERK1/2
tPEA15
1
6.32
1
1.52
G
MDA-MB-231,Sus, 24 h
PEA15: WT S116A
PD98059: - - +
LC3II
p62
Tubulin
1
2.28
1.87
1
9
5.52
H
LC3B/LAMP2
Pearson's Correlation Coefficient
**
***
WT
DMSO
PD98059
S116A
Pearson's correlation between LAMP2 and LC3
% Cells
</=0.5
> 0.5
WT
DMSO
PD98059
S116A
Sus, 24 h

Figure 6

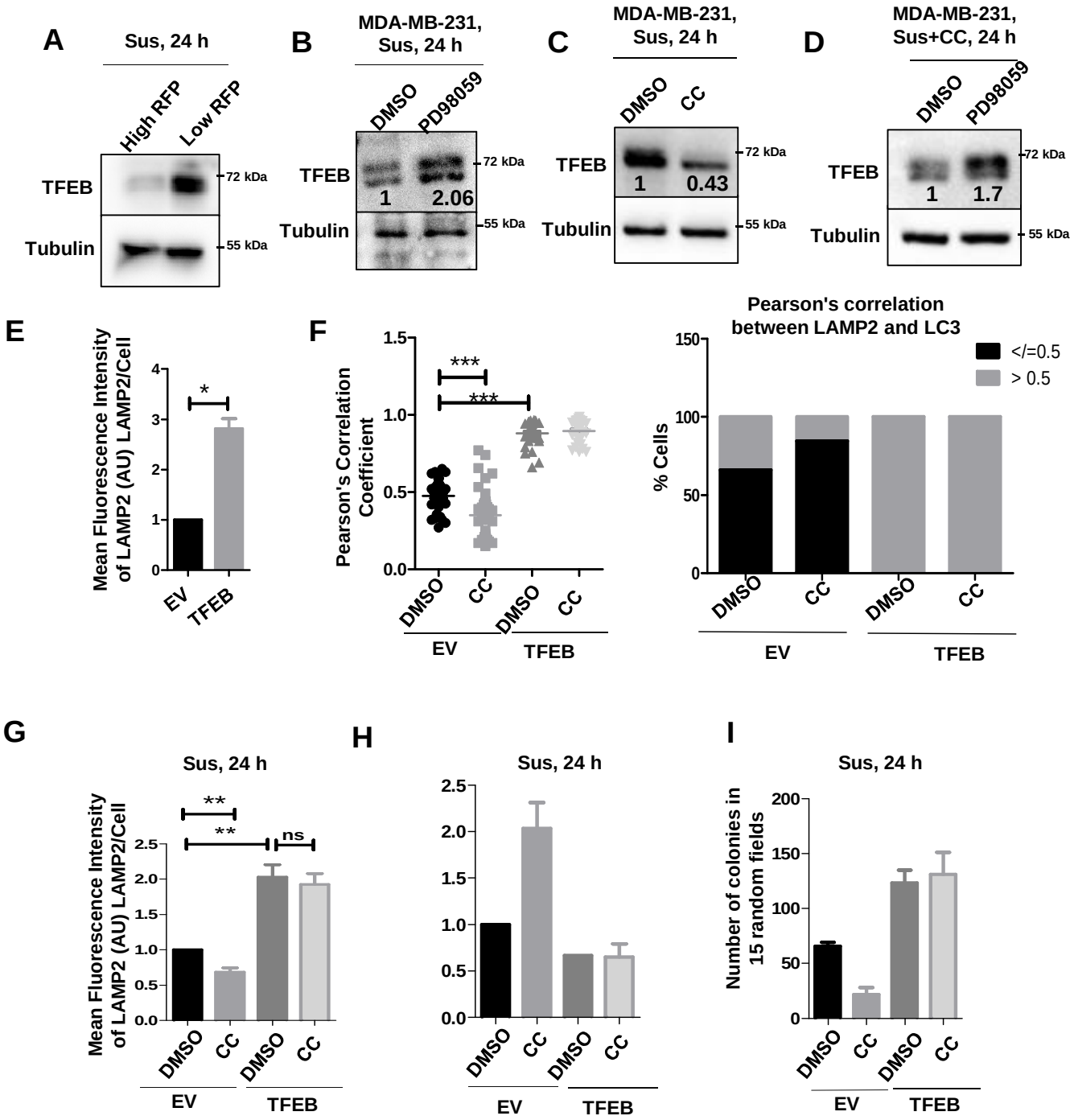
A
Sus, 24 h
High RFP
Low RFP
TFEB
Tubulin
72 kDa
55 kDa
B
MDA-MB-231, Sus, 24 h
DMSO
PD98059
TFEB
Tubulin
1
2.06
72 kDa
55 kDa
C
MDA-MB-231, Sus, 24 h
DMSO
CC
TFEB
Tubulin
1
0.43
72 kDa
55 kDa
D
MDA-MB-231, Sus+CC, 24 h
DMSO
PD98059
TFEB
Tubulin
1
1.7
72 kDa
55 kDa
E
Mean Fluorescence Intensity of LAMP2 (AU) LAMP2/Cell
*
EV
TFEB
F
Pearson's Correlation Coefficient
***
***
DMSO
CC
DMSO
CC
EV
TFEB
Pearson's correlation between LAMP2 and LC3
% Cells
</=0.5
> 0.5
DMSO
CC
DMSO
CC
EV
TFEB
G
Sus, 24 h
Mean Fluorescence Intensity of LAMP2 (AU) LAMP2/Cell
**
**
ns
DMSO
CC
DMSO
CC
EV
TFEB
H
Sus, 24 h
DMSO
CC
DMSO
CC
EV
TFEB
I
Sus, 24 h
Number of colonies in 15 random fields
DMSO
CC
DMSO
CC
EV
TFEB

Figure 7

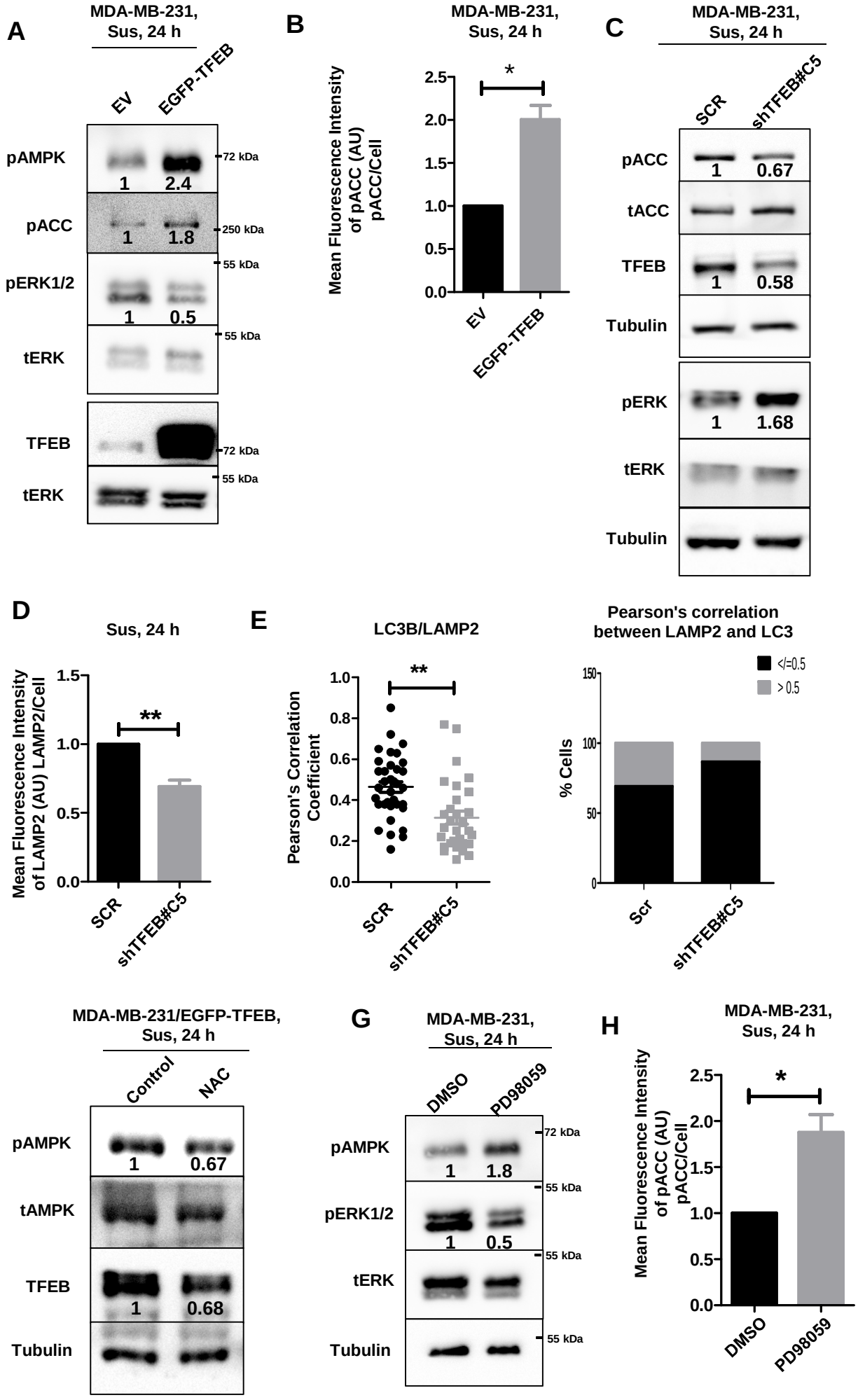
A
MDA-MB-231, Sus, 24 h
EV
EGFP-TFEB
pAMPK
1
2.4
72 kDa
pACC
1
1.8
250 kDa
pERK1/2
1
0.5
55 kDa
tERK
55 kDa
TFEB
72 kDa
tERK
55 kDa
B
MDA-MB-231, Sus, 24 h
Mean Fluorescence Intensity of pACC (AU) pACC/Cell
2.5
2.0
1.5
1.0
0.5
0.0
*
EV
EGFP-TFEB
C
MDA-MB-231, Sus, 24 h
SCR
shTFEB#C5
pACC
1
0.67
tACC
TFEB
1
0.58
Tubulin
pERK
1
1.68
tERK
Tubulin
D
Sus, 24 h
Mean Fluorescence Intensity of LAMP2 (AU) LAMP2/Cell
1.5
1.0
0.5
0.0
**
SCR
shTFEB#C5
E
LC3B/LAMP2
Pearson's Correlation Coefficient
1.0
0.8
0.6
0.4
0.2
0.0
**
SCR
shTFEB#C5
Pearson's correlation between LAMP2 and LC3
<=0.5
> 0.5
% Cells
150
100
50
0
Scr
shTFEB#C5
F
MDA-MB-231/EGFP-TFEB, Sus, 24 h
Control
NAC
pAMPK
1
0.67
tAMPK
TFEB
1
0.68
Tubulin
G
MDA-MB-231, Sus, 24 h
DMSO
PD98059
pAMPK
1
1.8
72 kDa
pERK1/2
1
0.5
55 kDa
tERK
55 kDa
Tubulin
55 kDa
H
MDA-MB-231, Sus, 24 h
Mean Fluorescence Intensity of pACC (AU) pACC/Cell
2.5
2.0
1.5
1.0
0.5
0.0
*
DMSO
PD98059

Figure 8

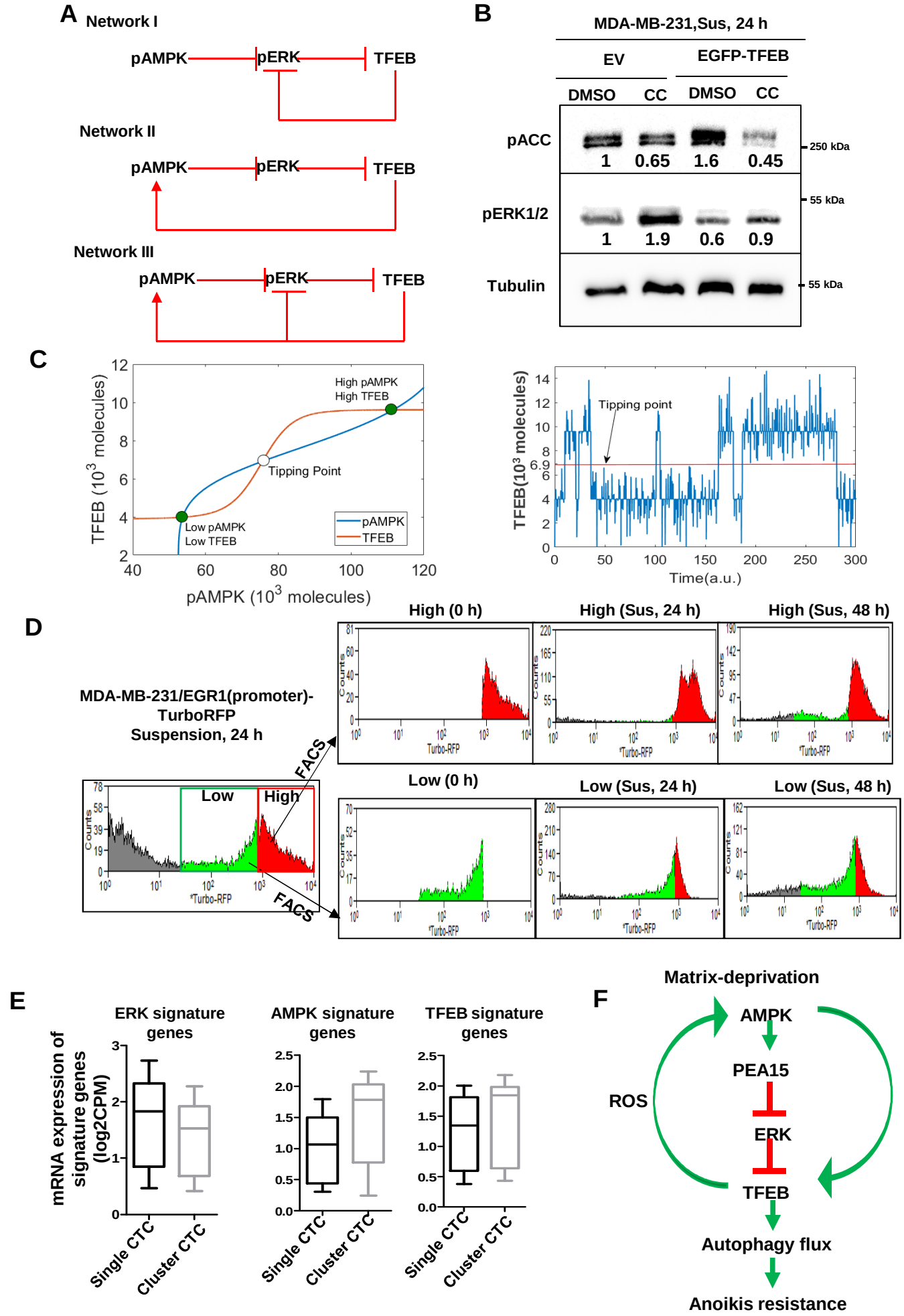
A
Network I
pAMPK
pERK
TFEB
Network II
pAMPK
pERK
TFEB
Network III
pAMPK
pERK
TFEB
B
MDA-MB-231,Sus, 24 h
EV
EGFP-TFEB
DMSO
CC
DMSO
CC
pACC
1
0.65
1.6
0.45
250 kDa
pERK1/2
1
1.9
0.6
0.9
55 kDa
Tubulin
55 kDa
C
High pAMPK
High TFEB
Tipping Point
Low pAMPK
Low TFEB
pAMPK
TFEB
TFEB (10^3 molecules)
pAMPK (10^3 molecules)
Tipping point
TFEB(10^3 molecules)
Time(a.u.)
D
MDA-MB-231/EGR1(promoter)-TurboRFP
Suspension, 24 h
Low
High
FACS
FACS
High (0 h)
High (Sus, 24 h)
High (Sus, 48 h)
Low (0 h)
Low (Sus, 24 h)
Low (Sus, 48 h)
Counts
Turbo-RFP
E
ERK signature genes
AMPK signature genes
TFEB signature genes
mRNA expression of signature genes (log2CPM)
Single CTC
Cluster CTC
F
Matrix-deprivation
AMPK
PEA15
ERK
TFEB
ROS
Autophagy flux
Anoikis resistance